

Anonymous Referee #1

The authors focused on the heterogeneous transformation of SO₂ on mineral dust during cloud processing by the simulated experiment. They characterized Fe morphology using the combined methods including TEM, Mossbauer, and CBD extraction method. The iron mobilized from mineral particle was also measured. Generally, heterogeneous transformation on the surface of mineral particle play a vital role on second particle formation. The result shown in this manuscript shed a light on heterogeneous chemistry, and it is helpful to further understand the fog and haze formation in China. Thus, this manuscript made some new contribution to atmosphere chemistry. The manuscript was well written and organized. The topic is of interest to the journal's readers. I thus recommended that this manuscript could be published on ACP. However, the manuscript also suffered from some flaws, and I listed as follows.

Thank the reviewer's chariness and suggestion. We appreciate the positive comments and suggestion about the manuscript. We agree with the reviewer's comments, and have updated the manuscript on the basis of these suggestions.

General questions/comments/suggestions:

1 The four examined clays were purchased from the clay mineral depository. The author should discuss why they were selected, particularly why they are representative of clays in aerosols.

Response: Clay is a more important component of mineral dusts. It was well documented that a long range transport would result in a decrease of quartz relative to the clay fraction because of the more rapid removal of quartz, which has the relatively larger mass median diameter of quartz (Mahowald et al., 2005). Dust deposition modeling showed that the clay fraction becomes more and more dominant on the downwind of the sources from Asia. In the African dust collected over Atlantic Ocean and Mediterranean, the clay group represented between 48 and 82% of the total aerosol mass, illite and kaolinite were the dominant minerals, smectite and chlorite were detected but in low concentrations (Journet et al., 2008). To explore the linkage between iron speciation in the clay minerals and properties of iron solubility, the typical Fe-containing clays, including the Fe-rich nontronite, illite and smectite were selected. Arizona test dust (ATD) is a commercially available material that has also

been widely studied as surrogate in the field of atmospheric chemistry and Fe chemistry.

The sentence has been added in line 55-58. “A long range transport would result in a decrease of quartz relative to the clay fraction because of the more rapid removal of quartz, hence clay is an important component of mineral dusts (Mahowald et al., 2005; Journet et al., 2008).”

The sentence in line 128 has been rewritten as “In this study, we employed four typical Fe-containing mineral samples as surrogates to perform simulated CP experiments.”

2 Line 159: “TEM observation”. The methods of TEM sample preparation will change the aggregation state of such aggregates. Some researchers have extensively worked on this and gave detailed information how they did it. Nothing is reported here on sample preparation. Therefore, please supply the detail about TEM sample.

Response: Thanks for the suggestion. We describe the TEM method in detail in line 214-221.

“Suspensions (0.2 g L^{-1}) of each particle were prepared in methanol and sonicated for at least 1 h. A drop of this suspension was then applied to a carbon-coated Cu TEM grid (400 mesh; EMS) and allowed to air-dry. The operation was conducted in bright field mode at 120 kV. The Fe content of the typical individual mineral particle were calculated from the values of 50 typical particles. To obviously observe the morphological changes, high-resolution TEM (HRTEM) images were also collected to observe nanoscale structural features, e.g., surface roughness and lattice fringes.”

3 The Fe_A and Fe_D content of Arizona Test Dust was “ $0.067 \pm 0.005\%$ for Fe_A and $0.41 \pm 0.04\%$ for Fe_D” in Shi et al. (2011), which was not completely in accordance with the values in Figure 4. The author should try to explain the discrepancy of Fe_A and Fe_D content.

Response: In the published paper of Shi et al., the Fe_A content ($0.067 \pm 0.005\%$) and Fe_D content ($0.41 \pm 0.04\%$) were the proportion of Fe_A and Fe_D per mass of dust, respectively. The total Fe content (Fe_T) of Arizona Test Dust (ATD) was 1.48%. The Fe_A/Fe_T and Fe_D/Fe_T was calculated to be $4.53 \pm 0.34\%$ and $27.70 \pm 2.70\%$, respectively, which were comparable to the values in this study, $3.8 \pm 0.3\%$ and $35.5 \pm 3.7\%$.

Further specific comments/suggestions: In Figure 3, please change the label “2 cycle” and “3 cycle” to “2 cycles” and “3 cycles”, respectively.

Response: We’ve changed the label “2 cycle” and “3 cycle” to “2 cycles” and “3 cycles” in Figure 3.

Remove some “the”, such as in Line 151.

Response: We’ve removed “the” in line 155.

Line 149, please comment on the rationale of the 1 g/L concentrations used in this experiment.

Response: The mineral particle samples are available in large amounts (g-kg) compared to atmospheric dust ($\mu\text{g-mg}$). These samples are clearly the precursor of atmospheric dusts prior to uplifting and thus have not been subject to changes that can happen to mineral dust in the atmosphere, allowing them to be used to investigate how these properties are modified during simulated atmospheric processing. Previous studies examined the iron dissolution over the range of dust loadings from 0.05 to 5 g/L in solutions. The solution with 1 g/L is usually representative for a cloud water solution.

Table 1 can be reported by both confirmation of sulfate ions origin (uptake vs H_2SO_4) and uptake coefficient (before vs after cloud processing).

Response: The IC measurements on sulfate ions released from mineral surface after CP were performed as blank experiments. The sulfate formation rates and uptake coefficients of SO_2 on particle samples after CP in Table 1 were recalculated by deduction of the blank value.

Line 381: Please replace “were” by “was”.

Response: The “were” has been replaced by “was” in line 412.

Line 376-377: This sentence contains partly the same data with the above sentences.

Response: Thanks for the reviewer’s suggestion. This sentence has been deleted in the revised manuscript.

Line 539: Please replace “during” by “by”.

Response: The “during” has been replaced by “by” in line 543.

Line 550-552: Is this a new result? or already known from other studies (then provide proper references)?

Response: This is a new result of our study.

In the References, Please exchange “Global Biogeochem, Cycles” by “Global Biogeochem. Cycles”.

Response: We’ve replaced “Global Biogeochem, Cycles” by “Global Biogeochem. Cycles”.

Anonymous Referee #2

General comments

The authors investigated heterogeneous uptake of sulfur dioxide on iron-containing mineral particles. They found enhanced heterogeneous uptake of sulfur dioxide on the mineral particles through modification of iron speciation. The results shown in this paper are very interesting. This study may provide additional pathway to promote the formation of sulfate in iron-containing aerosols. The manuscript is worthy of publication for ACP after some improvements to the readability.

We appreciate the positive comments and suggestion about the manuscript. We agree with the reviewer’s comments, and have updated the manuscript on the basis of these suggestion.

Specific comments

p.4, l.90: The reference of Ito et al. (2019) should be moved to previous sentence after Luo et al. (2008).

Response: The reference of Ito et al. (2019) has been moved to previous sentence after Luo et al. (2008) in line 91.

p.9, l.205: The formula of geometric area should be corrected.

Response: The formula of geometric area has been corrected as $A_{\text{geo}} = \text{mass} \times S_{\text{geo}}$ in line 209.

Table 1: The BET specific surface area is shown in Table S1. The unit and values of the total

surface area should be corrected.

Response: Thanks for the reviewer's correction. The unit and values of A_{BET} has been corrected in Table 1.

p.16, l.373 and Figure 3: Is the trend for ATD statistically significant? Please show the statistics.

Response: Although the simulated cloud processing experiment on each mineral was conducted three times to explore the change of Fe speciation after each pH cycle, the SO_2 uptake experiment was carried out only twice. At present, it was a pity that we don't have a trend for ATD statistically significant. Next, we'll do experiments more detailed.

Please discuss the results in subsection 3.2 with those in subsection 3.6 as is described in p.21, l.501. Subsection 3.2 may be moved at the end of section 3.

Response: Thanks for the suggestion. Because Figure 1 in subsection 3.2 demonstrated that the characteristic peaks for the active OH sites and the sulfite/sulfate products on the mineral particles after CP were significantly higher than those on the ones before CP, indicating the higher hygroscopicity and more SO_2 uptake on the particles after CP, which is the most direct evidence that CP could potentially promote the transformation of SO_2 on the particle surfaces. In order to emphasize the results and significance of this article, we tend to put subsection 3.2 at the first of section 3.

Subsection 3.4 may be combined with subsection 3.1.

Response: We agree with the reviewer's comment. We've combined subsection 3.4 with subsection 3.1 in line 273-308. Thus, the name of every subsection in section 3 has been correspondingly changed.

p.18, l.430: This has been already suggested by previous studies. Please cite references and rephrase the sentence. Subsection 3.5 may be moved to supplementary materials or before subsection 3.2.

Response: We've cited reference (Shi et al., 2009) and rephrased this sentence in line 432-436. "Previous research had indicated that Fe_A increased as a result of the simulated CP (Shi et al., 2009). Herein, we further proposed that the increased fractions of Fe_A could be mostly transformed from the "structural-Fe" in the aluminosilicate phase of the particles during CP, which is in good agreement with the TEM observation."

Subsection 3.5 is one of the most important content to inspect the Fe speciation before and after CP. We want to keep it in the manuscript.

p.20, 1.490: This has been already suggested by previous studies. Please cite references and rephrase the sentence. Subsection 3.6 may be moved to supplementary materials or before subsection 3.2.

Response: Herein, we've cited references and rephrased the sentence in line 494-495. "The fast Fe release was due to the redissolution of the Fe-rich precipitates, which was proposed to be reactive Fe phases (Shi et al., 2009; Shi et al., 2015)."

Subsection 3.6 "The dissolution-precipitation cycle of the mineral Fe during CP" is also one of the most important content to inspect the Fe speciation before and after CP. We tend to keep it in the manuscript.

p.22, 1.531: How did you know the particles were coated by reactive Fe? Please specify the relationship between the higher hygroscopicity and reactive Fe coating. Please show this evidence or rephrase the sentence.

Response: The dissolution-precipitation cycle of the mineral Fe was happened on the surface of particles. Additionally, the TEM observation confirmed that the nanosized Fe-rich crystal were attached onto the surface of ATD particles. These results help to confirm that the particles after CP were coated by reactive Fe.

To the best of our knowledge, there was no reports about the direct relationship between the higher hygroscopicity and reactive Fe coating. Previous studies have indicated that the reactive Fe could provide more surface hydroxyl species (OH) to participate in chemical reaction (Fu et al., 2007). In the study, the results of DRIFTS experiment demonstrated that the H₂O and OH groups on the surface of mineral particles significantly increased after CP, indicating the higher hygroscopicity of the particles after CP.

Therefore, we've rephrased the sentence in line 535-537. "The particle surfaces after CP were coated by these reactive Fe to provide more surface OH species, resulting in enhanced SO₂ uptake."

1 **Enhanced heterogeneous uptake of sulfur dioxide on**
2 **mineral particles through modification of iron speciation**
3 **during simulated cloud processing**

4 **Zhenzhen Wang¹, Tao Wang¹, Hongbo Fu^{1, 2, 3}, Liwu Zhang¹, Mingjin Tang⁴,**
5 **Christian George⁵, Vicki H. Grassian⁶, and Jianmin Chen¹**

6 ¹Shanghai Key Laboratory of Atmospheric Particle Pollution and Prevention,
7 Department of Environmental Science & Engineering, Institute of Atmospheric
8 Sciences, Fudan University, Shanghai, 200433, China

9 ²Shanghai Institute of Pollution Control and Ecological Security, Shanghai 200092,
10 China

11 ³Collaborative Innovation Center of Atmospheric Environment and Equipment
12 Technology (CICAEET), Nanjing University of Information Science and Technology,
13 Nanjing 210044, China

14 ⁴State Key Laboratory of Organic Geochemistry and Guangdong Key Laboratory of
15 Environmental Protection and Resources Utilization, Guangzhou Institute of
16 Geochemistry, Chinese Academy of Sciences, Guangzhou 510640, China

17 ⁵University of Lyon, Université Claude Bernard Lyon 1, CNRS, IRCELYON,
18 F-69626, Villeurbanne, France

19 ⁶Departments of Chemistry and Biochemistry, University of California, San Diego, La
20 Jolla, California 92093, United States

21 *Correspondence to:* Hongbo Fu (fuhb@fudan.edu.cn); Jianmin Chen
22 (jmchen@fudan.edu.cn)

23

24 **Abstract.** Iron-containing mineral aerosols play a key role in the oxidation of sulfur
25 species in the atmosphere. Simulated cloud processing (CP) of typical mineral
26 particles, such as illite (IMt-2), nontronite (NAu-2), smectite (SWy-2) and Arizona
27 test dust (ATD) is shown here to modify sulfur dioxide (SO₂) uptake onto mineral
28 surfaces. Heterogeneous oxidation of SO₂ on particle surfaces was firstly investigated
29 using an *in situ* DRIFTS apparatus. Our results showed that the BET surface area
30 normalized uptake coefficients (γ_{BET}) of SO₂ on the IMt-2, NAu-2, SWy-2 and ATD
31 samples after CP were 2.2, 4.1, 1.5 and 1.4 times higher than the corresponding ones
32 before CP, respectively. The DRIFTS results suggested that CP increased the amounts
33 of reactive sites (e.g., surface OH groups) on the particle surfaces and thus enhanced
34 the uptake of SO₂. TEM showed that the particles broke up into smaller pieces after
35 CP, and thus produced more active sites. The “free-Fe” measurements confirmed that
36 more reactive Fe species were present after CP, which could enhance the SO₂ uptake
37 more effectively. Mössbauer spectroscopy further revealed that the formed Fe phase
38 were amorphous Fe(III) and nanosized ferrihydrite hybridized with Al/Si, which were
39 possibly transformed from the Fe in the aluminosilicate lattice. The modification of
40 Fe speciation was driven by the pH-dependent fluctuation coupling with Fe
41 dissolution-precipitation repeatedly during the experiment. Considering both the
42 enhanced SO₂ uptake and subsequent promotion of iron dissolution along with more
43 active Fe formation, which in turn lead to more SO₂ uptake, it was proposed that there
44 may be a positive feedback between SO₂ uptake and iron mobilized on particle
45 surfaces during CP, thereby affecting climate and biogeochemical cycles. This
46 self-amplifying mechanism generated on the particle surfaces may also serve as the
47 basis of high sulfate loading in severe fog-haze events observed recently in China.

48

49 1 Introduction

50 Mineral dust is a major fraction of global atmospheric aerosol budget, with an
51 estimated annual emission flux of 1000 to 3000 Tg into the atmosphere (Jickells et al.,
52 2005; Andreae and Rosenfeld, 2008). Mineral dust aerosol mainly consists of quartz,
53 feldspars, carbonates (calcite, dolomite), and clay minerals (illite, kaolinite, chlorite,
54 montmorillonite), the exact composition varies with source (Claquin et al., 1999;
55 Formenti et al., 2008). A long range transport would result in a decrease of quartz
56 relative to the clay fraction because of the more rapid removal of quartz, hence clay is
57 an important component of mineral dusts (Mahowald et al., 2005; Journet et al., 2008).
58 During the long-range transport, mineral dust provides a reactive surface for
59 heterogeneous chemistry (Zhang et al., 2006; George et al., 2015; Huang et al., 2015).
60 Heterogeneous reactions of atmospheric trace gases on mineral dust particles are of
61 great significance as these reactions alter the chemical balance of the atmosphere and
62 modify the properties of individual particles (Usher et al., 2003; Wu et al., 2011;
63 Huang et al., 2015).

64 SO₂ is an important trace gas, which is released mainly by fossil fuel combustion
65 and volcanic emission. The heterogeneous conversion of SO₂ on mineral dust surfaces
66 leads to the formation of sulfuric acid and sulfate aerosols, resulting in a significant
67 cooling effect on the global climate by scattering solar radiation and acting as cloud
68 condensation nuclei (CCN) to affect climate indirectly (Lelieveld and Heintzenberg,
69 1992; Usher et al., 2003; Kolb et al., 2010). In addition, sulfate containing particles
70 play a significant role in the haze formation in China in recent years (Sun et al., 2014;
71 Wang et al., 2014; Yang et al., 2017). SO₂ can be gaseous oxidized to sulfate by OH
72 radical, and be aqueous oxidation in cloud and fog droplets by ozone and hydrogen
73 peroxide (Luria and Sievering, 1991), or through heterogeneous processes that occur

74 on aerosol particle surfaces (Usher et al., 2003; Ullerstam et al., 2003). However, the
75 high sulfate levels measured in recent field observations cannot be explained by
76 current atmospheric models (Kerminen et al., 2000; Wang et al., 2003; Cheng et al.,
77 2016), leading to a large gap between the modeled and field-observed sulfate
78 concentrations using known oxidation pathways (Herman, 1991; Kasibhatla et al.,
79 1997; Barrie et al., 2016). Overall, on a global scale, atmospheric SO₂ concentration
80 were typically overestimated, while sulfate tended to be underestimated, suggesting
81 missing sulfate production pathways (Harris et al., 2013; Kong et al., 2014).

82 It has been suggested that the heterogeneous conversion of SO₂ could make an
83 important contribution to the atmospheric sulfate loading. Laboratory studies typically
84 focus on SO₂ uptake onto a variety of metal oxides and mineral particles (Goodman et
85 al., 2001; Usher et al., 2002; Zhao et al., 2015; Yang et al., 2016), and have confirmed
86 that its conversion rate on the surface of Fe (hydr)oxides was faster compared to other
87 metal oxides investigated, in good agreement with the field-measurement (Usher et al.,
88 2002; Zhang et al., 2006). Atmospheric Fe is emitted from both anthropogenic
89 (primarily biomass burning, coal and oil combustion) and natural (mineral dust and
90 volcanic ash) sources, with the mineral dust source dominant globally (Siefert et al.,
91 1998; Luo et al., 2008; [Ito et al., 2019](#)). It has been established that an important in
92 cloud S (IV) oxidation pathway is catalyzed by natural transition metal ions,
93 especially Fe hosted within mineral particles (Alexander et al., 2009; Harris et al.,
94 2013).

95 Another important consideration for heterogeneous chemistry of mineral dust
96 aerosol, is how mineral dust particles change in the atmosphere. During long-range
97 transport, mineral particles often undergo chemical ageing by atmospheric processes
98 (Mahowald et al., 2005; Baker and Croot, 2010; Shi et al., 2011). Cloud processing

删除的内容: ; Ito et al., 2019

100 involves cloud water condensation and evaporation on the particle surfaces, along
101 with drastic liquid water content and pH fluctuations (Mackie, 2005; Shi et al., 2011;
102 Rubasinghege et al., 2016). During CP, the high relative humidity (RH) results in high
103 aerosol water content and relatively high pH (Behra et al., 1989; Baker and Croot,
104 2010; Shi et al., 2011). While water evaporation from cloud droplets to wet aerosol at
105 higher temperature, the particles only contain a concentrated aqueous aerosol solution,
106 in which the pH can be lower than 2 (Zhu et al., 1993; Meskhidze, 2003; Shi et al.,
107 2015). Therefore, there is a highly acidic film (e.g., pH = 2) in the “wet aerosol” phase
108 versus a less acidic droplet (near-neutral, 5-6) in the “cloud droplet” phase within
109 clouds (Shi et al., 2015). During its lifetime, a typical aerosol particle may experience
110 several cloud cycles involving large pH variations before being removed from the
111 atmosphere as rain or through dry deposition (Pruppacher and Jaenicke, 1995; Maters
112 et al., 2016). Herein, the simulated CP experiment was conducted by changing pH
113 between 2 and 5-6, in accordance with the previous studies (Spokes et al., 1994;
114 Mackie, 2005; Shi et al., 2009).

115 It was well documented that pH is especially important for Fe mobilization (Zhu et
116 al., 1993; Desboeufs et al., 2001; Deguillaume et al., 2010; Maters et al., 2016). The
117 fluctuating pH during CP will impact and change the Fe speciation and morphology in
118 dust particles (Zhuang et al., 1992; Wurzler et al., 2000; Shi et al., 2009; Kadar et al.,
119 2014). The low pH will increase Fe solubility and bioavailability of dust during
120 transport, thereby providing Fe external input to the open ocean surface to promote
121 marine prime productivity (Spokes et al., 1994; Desboeufs et al., 2001). It has been
122 found that Fe-rich nanoparticle aggregates were formed from Saharan soil and
123 goethite upon simulated CP conditions, in good agreement with their
124 field-measurements from the wet-deposited Saharan dusts collected from the western

125 Mediterranean (Shi et al., 2009). Fe nanoparticles are more chemically reactive
126 (Wurzler et al., 2000; Desboeufs et al., 2001), possibly lead to a remarkable difference
127 in heterogeneous chemistry. However, little is known about the influence of CP on
128 SO₂ uptake onto particle surfaces up to now.

129 In this study, we employed four typical Fe-containing mineral samples as
130 surrogates to perform simulated CP experiments. The SO₂ uptakes on the mineral
131 particles before and after CP were compared using *in situ* diffuse reflectance infrared
132 Fourier transform spectroscopy (DRIFTS). Transmission electron microscopy (TEM)
133 was applied to observe the morphological and mineralogical change of mineral
134 particles. The Fe speciation modification during simulated CP was further monitored
135 by the dissolved Fe measurement, the “free-Fe” analysis and Mössbauer spectroscopic
136 characterization.

137 **2 Material and methods**

138 **2.1 Mineral particles**

139 The standard mineral samples of IMt-2, NAu-2 and SWy-2 were purchased from
140 the Source Clay Minerals Repository (Purdue University, West Lafayette, IN). ATD
141 was purchased from Powder Technology Inc. (Burnsville, MN, USA). The mineral
142 samples were coarsely ground using a mortar and pestle before being more finely
143 ground using an All-dimensional Planetary Ball Mill QM-QX (Nanjing University
144 Instrument Plant) and were sieved to particle diameters (D_p) < 45 μm prior to analysis.
145 The Brunauer-Emmett-Teller specific surface areas (S_{BET}) of the samples were
146 measured with a Quantachrome Nova 1200 BET apparatus. Total iron content (Fe_T) of
147 the samples were determined using an inductively coupled plasma atomic emission
148 spectroscopy (ICP-AES, Jobin Yvon Ultima). The chemical compositions of the
149 particles were analyzed by X-ray fluorescence spectrometry (XRF, PANalytical Axios

150 Advanced).

151 2.2 Cloud processing simulation experiment

152 The simulated CP experiments were conducted at a constant temperature ($298 \pm 1\text{K}$)
153 using a Pyrex glass vessel with a water jacket. The suspensions contained a mineral
154 particle loading of 1 g L^{-1} were subjected to acidic ($\text{pH} = 2 \pm 0.1$, 24 h) and
155 near-neutral pH ($\text{pH} = 5\text{-}6$, 24 h) cycles for 1-3 times according to the previous
156 methods (Spokes et al., 1994; Mackie, 2005; Shi et al., 2009). Suspension pH was
157 adjusted by adding dilute H_2SO_4 or NH_4OH . The CaCO_3 equivalent alkalinity of the
158 dust was determined in accordance with APHA method 2320B so that acid additions
159 to control pH could be adjusted accordingly (Mackie, 2005). The amount of acid or
160 alkali added to achieve these pH cycles was less than 1% of the total volume of the
161 suspensions. The experiments were performed under a constant stirring (about 50
162 rpm) in the dark for 144 h. At the end of the CP experiment, the suspensions were
163 filtered through $0.2\ \mu\text{m}$ PTFE filters (Millipore). The filter residue was air-dried, and
164 was further applied to the DRIFTS experiment, as well as TEM observation, “free-Fe”
165 measurement and Mössbauer spectroscopic characterization.

166 2.3 SO_2 uptake on the mineral particles

167 The SO_2 uptake on the particle surfaces before and after CP was investigated by a
168 Shimadzu Tracer-100 FTIR spectrometer equipped with a high-sensitivity mercury
169 cadmium telluride (MCT) detector and a diffuse reflectance accessory. A temperature
170 controller was fitted to the DRIFTS chamber to ensure constant reaction temperature
171 (298 K). Weighted sample was placed into a ceramic crucible (0.35 mm depth, 5 mm i.
172 d.) in the chamber. Mass flow controllers (Beijing Sevenstar electronics Co., LTD)
173 were used to adjust the reactant gases to a flux with expected concentration and
174 relative humidity. The sample was firstly pretreated in a 100 mL min^{-1} flow of

删除的内容: The s

176 synthetic air (21% O₂ and 79% N₂) for 1 h to blow off water and impurities on
177 particle surface. When the background spectrum of the fresh sample reached steady
178 state, the reactant gas of SO₂ (5.0 ppm) along with synthetic air was introduced into
179 the chamber at a total flow rate of 120 mL min⁻¹ for 45 min, during which the IR
180 spectrum was recorded automatically every 5 min at a resolution of 4 cm⁻¹ for 100
181 scans in the spectral range of 900 to 4000 cm⁻¹. Atmospheric moisture was simulated
182 with a RH level around 40 % by guiding one high-pure air flux through water. The
183 humidity value was monitored using a hygrometer.

184 The sulfate products were analyzed by ion chromatography (IC) after the DRIFTS
185 experiments. The particles were extracted with 5 ml ultrapure water by ultrasonic
186 extractor. After 10 min, the extracted solution was passed through a 0.22 μm PTFE
187 membrane filter and the leaching solution was analyzed using a Metrohm 883 Basic
188 IC equipped with an A5-250 column. A weak base eluent (3.2 mmol L⁻¹ Na₂CO₃ plus
189 1.0 mmol L⁻¹ NaHCO₃) was used for anion detection at a flow rate of 0.70 ml min⁻¹.
190 To discriminate the adsorbed sulfate during simulated CP experiment and the sulfate
191 ions generated from the heterogeneous reaction, the adsorbed sulfate on the particles
192 during simulated CP experiment were initially measured as blank. The heterogeneous
193 uptake of SO₂ was calculated by subtracting the blank value from the total sulfate
194 ions.

195 The reactive uptake coefficient (γ) was defined as the rate of sulfate formation on
196 the surface ($d[\text{SO}_4^{2-}]/dt$, ions s⁻¹) divided by collision frequency (Z , molecules s⁻¹)
197 (Usher et al., 2003; Ullerstam et al., 2003; Kong et al., 2014; Huang et al., 2015).

$$198 \quad \gamma = \frac{d[\text{SO}_4^{2-}]/dt}{Z}, \quad (1)$$

$$199 \quad Z = \frac{1}{4} \times A_s \times [\text{SO}_2] \times v, \quad (2)$$

200
$$v = \sqrt{\frac{8RT}{\pi M_{SO_2}}}, \quad (3)$$

201 Where, A_s is the effective sample surface of the samples, m^2 ; v is the mean
202 molecular velocity of SO_2 , $m \cdot s^{-1}$; R is the gas constant, $J \cdot mol^{-1} \cdot K^{-1}$; T is the absolute
203 temperature, K ; and M_{SO_2} is the molecular weight of SO_2 , $kg \cdot mol^{-1}$.

204 A conversion factor was obtained by a calibration plot with numbers of SO_4^{2-}
205 analyzed by ion chromatography (IC, Metrohm 883 Basic, Switzerland) versus the
206 integrated areas of sulfate products from DRIFTS spectra. The residual sulfate during
207 simulated CP experiments were deducted as background. The calculated conversion
208 factor of SO_4^{2-} is 1.170×10^{15} (ions \cdot integrated units $^{-1}$). Integrated areas for the total
209 sulfur-containing products were calculated to show the maximal sulfate formation
210 rates. The reactive uptake coefficient for SO_2 was determined to be γ_{BET} and γ_{geo} using
211 the BET area ($A_{BET} = mass \times S_{BET}$) and geometric area ($A_{geo} = mass \times S_{geo}$) as the
212 reactive area, respectively.

删除的内容: S_{BET}

213 2.4 Morphological and mineralogical characterization of the Fe speciation

214 A FEI TECNAI G2 S-TWIN F20 TEM equipped with an Oxford energy-dispersive
215 X-ray spectrometer (EDX) was used to analyze the morphological and chemical
216 composition of individual particles before and after CP. Suspensions (0.2 g L^{-1}) of
217 each particle were prepared in methanol and sonicated for at least 1 h. A drop of this
218 suspension was then applied to a carbon-coated Cu TEM grid (400 mesh; EMS) and
219 allowed to air-dry. The operation was conducted in bright field mode at 120 kV. The
220 Fe content of the typical individual mineral particle were calculated from the values
221 of 50 typical particles. To obviously observe the morphological changes,
222 high-resolution TEM (HRTEM) images were also collected to observe nanoscale
223 structural features, e.g., surface roughness and lattice fringes.

删除的内容: A drop of this suspension was then applied to a carbon-coated Cu TEM grid (400 mesh; EMS). A FEI TECNAI G2 S-TWIN F20 TEM equipped with an Oxford energy-dispersive X-ray spectrometer (EDX) was used for high-resolution imaging and to analyze the chemical composition of individual particles. The Fe content of the typical individual mineral particle were calculated from the values of 50 typical particles. Selected area electron diffraction (SAED) was used to identify the crystalline phases.

233 The content of “free-Fe” in the mineral particles was determined by a
234 citrate-buffered-dithionite (CBD) sequential Fe extractions method according to the
235 literature (Lafon et al., 2004; Shi et al., 2009). Simply, 30 mg of the dust samples
236 were treated for 24 h with a 10 mL ascorbate solution (pH = 7.5) to extract chemically
237 highly labile Fe phases (Fe_A), mainly composed of amorphous, nanoparticle and/or
238 poorly crystalline ferrihydrite. The solutions were filtered through 0.2 μm
239 polycarbonate filters. The dust particles collected on the filters were subsequently
240 treated for 2 h with a 10 mL sodium dithionite solution (pH = 4.8) to extract
241 crystalline Fe (oxyhydr) oxides (Fe_D), which are mainly goethite and hematite. After
242 each reaction step, the dissolved Fe concentrations (Fe_A and Fe_D) in the filtrates were
243 determined using ICP-AES. The sum of these two pools ($Fe_A + Fe_D$) was defined as
244 the “free-Fe” fraction (Shi et al., 2011). The other fraction was donated as the
245 “structural-Fe” in aluminosilicate crystals, which could be calculated from the
246 difference between the Fe_T and “free-Fe” fractions (Lafon et al., 2004).

247 The Mössbauer spectroscopic analysis performed in transmission geometry with a
248 constant acceleration was used to inspect the chemical valence and the surrounding
249 structure of Fe in the particles before and after CP. ^{57}Co was used as the Mössbauer
250 source, and a 1 mm thick Na(Tl) scintillator coupled to a EMI9750B photoelectric
251 multiplier was used as the detector (Cwiertny et al., 2008). The measurement was
252 carried out at room temperature (RT) with a duration of 24 hours for one sample
253 (around 1.5×10^6 counts per channel). Experimental data were fitted by a least-squares
254 fitting-program. The isomer shift values were calibrated against a spectrum for α -Fe
255 metal foil.

256 During the simulated CP experiment, the total dissolved iron (Fe_s) and the dissolved
257 Fe(II) in the suspensions were measured colorimetrically by the Ferrozine method, as

258 described in previous studies (Viollier et al., 2000; Cwiertny et al., 2008). For Fe(II)
259 analysis, 200 mL of a 5 mM 1, 10-phenanthroline solution and 200 mL of an
260 ammonium acetate buffer were added into 1 mL of sample. To avoid possible
261 interference from Fe(III), which can also form a complex with 1,10-phenanthroline
262 when present at high concentrations, 50 mL of 0.43 M ammonium fluoride was added
263 to the sample prior to 1,10-phenanthroline. The mixture was allowed to sit in the dark
264 for 30 min prior to ultraviolet-visible spectroscopy (UV-Vis) analysis, during which
265 time a reddish-orange color developed if Fe(II) was present. Fe_s was determined via
266 the same protocol, except that 20 mL of 1.5 M hydroquinone, which reduces Fe(III) to
267 Fe(II), was added to the sample rather than ammonium fluoride. Absorbance
268 measured at 510 nm was converted to concentrations using aqueous standards
269 prepared from anhydrous beads of ferrous chloride. Standards were prepared in each
270 acid used in dissolution studies, and no matrix effects were observed. These
271 conditions resulted in a detection limit of 1 μ M. The concentration of dissolved
272 Fe(III) was calculated from the difference in experimentally measured concentrations
273 of total dissolved iron and dissolved Fe(II).

274 Additionally, the dissolved Fe(III) could precipitate out as the pH increased, and
275 then the Fe mineralogy of the deposit was also observed. NAu-2 released about
276 300 μ M of dissolved Fe at pH 2. The dissolving solution (200 mL) was sampled
277 after filtration (0.2 μ m polycarbonate filter). The clear solution was subjected to
278 changing acidity from pH 2 to 5 by the stepwise addition of dilute NH₄OH. The
279 precipitated particles were separated out by 0.2 μ m filters and were used in TEM
280 and Mössbauer analysis. Size distributions for the Fe-bearing particles formed in
281 the suspensions were determined by a Horiba LB-500 light scattering microscopy
282 within the size range of 3-6000 nm.

283 3 Results and discussion

284 3.1 Morphological change of the mineral particles after CP,

删除的内容: Characterization of mineral samples

285 The characteristic results are shown in Table S1 and Table S2. The samples
286 exhibited S_{BET} in the range from 4.3 ± 0.3 to 22.6 ± 2.3 m²/g. The Fe_T content were
287 $5.45 \pm 0.34\%$, $26.30 \pm 0.57\%$, $2.36 \pm 0.56\%$ and $1.48 \pm 0.56\%$, for IMt-2, NAu-2,
288 SWy-2 and ATD, respectively. The proportions of Fe₂O₃ in IMt-2, NAu-2, SWy-2
289 and ATD were 7.95%, 39.03%, 5.55% and 2.57%, respectively.

290 Figure 1 shows the TEM images of the mineral particles before and after CP. As
291 shown in Figure 1 a, c, e and g, the IMt-2, NAu-2, SWy-2 and ATD samples before
292 CP primarily consisted of laminar aluminosilicate with irregular shape and rough
293 morphologies mainly at the micrometer scale, all of which were characterized by
294 various fractions of Fe (1.5%-26.2%), along with minor Mg (0.1%-16.5%), K
295 (0.0%-7.8%) and Ca (0.0%-1.1%). The Fe within the aluminosilicates of the particles
296 was evenly distributed. Besides, some Fe-rich crystal with several hundreds of
297 nanometers in size were found to attach onto the ATD particles, which were identified
298 as α -Fe₂O₃ (PDF: 33-664) from the typical *d*-spacing analysis of HRTEM (Janney et
299 al., 2000).

已移动 (插入) [1]

删除的内容: 4

删除的内容: 4

300 After the simulated CP, all of the processed mineral particles showed much smaller
301 size than the ones before CP. For example, the typical IMt-2 and NAu-2 particles after
302 CP (Figure 1 b and d) were $< 1 \mu\text{m}$ in size. Under the TEM, the average Fe content of
303 the individual IMt-2 and SWy-2 particles (Figure 1 b and f) decreased from 5.5% (\pm
304 1.9%; $n = 50$) to 4.1% ($\pm 1.6\%$; $n = 50$) and from 2.4% ($\pm 0.6\%$; $n = 50$) to 2.1% (\pm
305 0.5%; $n = 50$), respectively. In addition, the IMt-2 particles after CP showed a
306 heterogeneous distribution of the Fe on the basis of the EDX data. Most of the
307 aluminosilicate in IMt-2 after CP hosted lower Fe content (4.1%), whereas a few of

删除的内容: 4

删除的内容: 4

313 the Fe-rich particles with less Si/Al were observed with irregular shapes at the
314 nanoscale. The TEM images of the NAu-2 and ATD particles after CP (Figure 1 h)
315 showed some pseudo-hexagonal nanoparticles with around 5 nm in diameter. Based on
316 the EDX and SAED analysis, these nanoparticles were Fe-rich and the *d*-spacings was
317 at about 1.5-2.5 Å, all of which were identified to be 2-line ferrihydrite (Janney et al.,
318 2000; Shi et al., 2009).

删除的内容: 4

319 The TEM observation suggested that CP induced the disintegration of mineral
320 particles and thus produced enhanced surface area, resulting in more active sites
321 available on the particle surfaces for SO₂ uptake. Results of TEM also showed that CP
322 influenced the Fe mineralogy, and lead to the Fe-rich nanoparticle formation, which
323 could partly explain the higher SO₂ uptake on the mineral particles after CP.

324 **Figure 1**

删除的内容: 4

325 **3.2 Effect of simulated CP on heterogeneous transformation of SO₂**

326 The *in situ* DRIFTS spectra on the IMt-2, NAu-2, SWy-2 and ATD samples before
327 and after CP exposed to SO₂ as a function of time are shown in Figure 2. For the
328 IMt-2 sample before CP (Figure 2a and b), the intensities of the broad peaks from
329 3600 to 3000 cm⁻¹ and a weak peak at 1650 cm⁻¹ increased with time. The band
330 between 3600 and 3000 cm⁻¹ was attributed to the vibrations of hydrogen-bonded
331 hydroxyl species (Zhao et al., 2015), while the absorption peak at 1650 cm⁻¹ was
332 mainly associated to H₂O produced from the reaction between SO₂ and surface
333 hydroxyls (Nanayakkara et al., 2012; Cheng et al., 2016). A weak vibration was
334 observed at around 1100 cm⁻¹, which might be attributed to free sulfate anions on the
335 particle surface (Ullerstam et al., 2003; Nanayakkara et al., 2012; Yang et al., 2016).
336 Previous studies established that various types of surface OH groups are the key
337 reactive sites for sulfite/sulfate and bisulfite/bisulfate formation on mineral oxides

删除的内容: 1

删除的内容: 1a

删除的内容: 1

343 (Faust et al., 1989; Usher et al., 2003; Ullerstam et al., 2003), because of the
344 complexes formed between sulfite/sulfate species and the surface OH. Generally, the
345 SO₂ adsorption grow in intensity with decreasing OH stretching and H₂O banding
346 (Zhang et al., 2006). However, the OH peaks herein were not observed to decrease
347 with prolonged time, because the losses of H₂O and OH groups on the particle
348 surfaces were replenished by maintaining the constant RH in this study.

349 When the same set of experiments were carried out using the IMt-2 sample after CP
350 (Figure 2b), the intensities of the prominent peaks were significantly higher than those
351 on the IMt-2 sample before CP. Four new bands were readily observed at 1167, 1100,
352 1088 and 1077 cm⁻¹. The new bands were easily assigned to the stretching motion of
353 surface-coordinated sulfate species (1167 cm⁻¹), i.e., bidentate surface sulfate
354 complexes, free sulfate ion (1100 cm⁻¹), and sulfite/bisulfite species (1088 and 1077
355 cm⁻¹) (Peak et al., 1999; Ullerstam et al., 2003; Yang et al., 2016). These new bands
356 remained when an argon blow-off process was carried out, suggesting that the
357 surface-adsorbed sulfite/sulfate species between 1250 and 1000 cm⁻¹ was
358 chemisorbed (Zhang et al., 2006).

359 Upon adsorption of SO₂ on the surface of the NAu-2 sample before CP (Figure 2c
360 and d), the broad band from 3600 to 2800 cm⁻¹ and the peaks at 1580 and 1675 cm⁻¹
361 increased drastically with time. These absorbance bands were all attributed to the
362 surface hydroxyl species (OH) and H₂O. No peaks were observed over the range of
363 1000 to 1250 cm⁻¹, suggesting that the sulfite/sulfate products were not formed newly
364 on the surface of the NAu-2 sample before CP. Upon adsorption of SO₂ on the surface
365 of the NAu-2 sample after CP (Figure 2d), the new bands at 3661 and 3450 cm⁻¹, the
366 broad band between 3400 and 2700 cm⁻¹, and the broad band centered at 2131 cm⁻¹,
367 were observed as the exposure time increased. In detail, the band at 3661 cm⁻¹ could

删除的内容: 1b

删除的内容: 1c

删除的内容: 1d

删除的内容: 1d

372 be assigned to stretching vibration modes of isolated or bridged surface hydroxyl
373 groups bonded to the surface iron ions embedded in the octahedral and tetrahedral
374 sites (Faust et al., 1989; Nanayakkara et al., 2012; Zhao et al., 2015). The peaks at
375 around 3450 cm^{-1} , 2131 cm^{-1} and the band between 3400 and 2700 cm^{-1} were all
376 attributed to surface OH groups (Ma et al., 2010; Zhao et al., 2017). These new bands
377 generated on the processed N Au-2 particles suggested that CP changed the location of
378 diverse OH groups on the particle surfaces. Over the range of 1250-1000 cm^{-1} , the
379 new bands centered at 1170 cm^{-1} was assigned to the asymmetric stretching of sulfate
380 (Kong et al., 2014; Yang et al., 2015).

381 The spectra of the SWy-2 samples before and after CP (Figure 2e and f) showed a
382 similar spectral character with those of the N Au-2 samples. The spectra for the ATD
383 samples before and after CP (Figure 2g and h) were roughly the same as the ones for
384 IMt-2. All of the results demonstrated that the characteristic peaks for the active OH
385 sites and the sulfite/sulfate products on the mineral particles after CP were
386 significantly higher than those on the ones before CP, indicating the higher
387 hygroscopicity and more SO_2 uptake on the particles after CP. The data shown herein
388 confirmed that CP could potentially promote the transformation of SO_2 on the particle
389 surfaces.

390 **Figure 2**
391 **3.3 Uptake coefficient of SO_2 on the mineral particles before and after CP**

392 The areas of the bands (from 1250 to 1000 cm^{-1}) attributed to the sulfite/sulfate
393 products as a function of time are shown in Figure 3. It was evident that the peak
394 areas of the products on the mineral particles after CP were generally greater than the
395 ones before CP. The reaction on the sample surfaces was practically saturated to SO_2
396 uptake within 15 min, except for the N Au-2 and IMt-2 samples after CP. As for all of

删除的内容: 1e

删除的内容: 1

删除的内容: 1

删除的内容: 2

401 the sample, the saturation coverages of the sulfite/sulfate products after CP were
402 obviously greater than the corresponding values before CP, suggesting that CP
403 favored the sulfate formation on the mineral surfaces due to improving active site
404 number, as expected previously.

405 **Figure 3**

删除的内容: 2

406 The maximum uptake coefficients (γ_{geo} and γ_{BET}) for SO_2 uptake on the samples
407 were estimated on the basis of the sulfate formation rates in the initial 15 min. The
408 values on the mineral samples before and after CP are shown in Table 1. The γ_{geo}
409 values of SO_2 on the IMt-2, N Au-2, SWy-2 and ATD samples before CP were
410 1.03×10^{-7} , 0.30×10^{-7} , 1.72×10^{-7} and 1.37×10^{-7} , respectively, which were in the order
411 of SWy-2, ATD, IMt-2 and N Au-2. The γ_{geo} values of SO_2 on the IMt-2, N Au-2,
412 SWy-2 and ATD samples after CP were 4.7, 19.4, 2.7 and 2.0 times higher than the
413 values before CP, respectively, suggesting that the SO_2 uptake on the mineral particles
414 significantly increased after CP.

415 **Table 1**

带格式的: 孤行控制, 调整中文与西文文字的间距, 调整中文与数字的间距

416 A_{BET} was more appropriate to represent the effective area, because the reactant may
417 diffuse into tiny holes of the entire sample. The γ_{BET} values of SO_2 on the IMt-2,
418 N Au-2, SWy-2 and ATD samples before CP were 2.62×10^{-12} , 0.75×10^{-12} , 3.70×10^{-12}
419 and 1.61×10^{-11} , respectively, which were in the order of ATD, SWy-2, IMt-2 and
420 N Au-2. It was noteworthy that the S_{BET} of samples increased after CP, as shown in
421 Table 1. The γ_{BET} values of SO_2 on the IMt-2, N Au-2, SWy-2 and ATD after CP were
422 2.2, 4.1, 1.5 and 1.4 times higher than the values before CP, respectively. The
423 discrepancies in the γ_{BET} value confirmed that the higher sulfate formation rates of the
424 particles after CP was not only due to the increased surface area of the particles, but
425 also resulting from the chemical modification on the particle surfaces.

带格式的: 字体: 小四

427 The estimated uptake coefficients were several orders of magnitude lower than the
428 results from Ullerstam et al. (2003) and Usher et al. (2003), which could be partly
429 explained by the difference in the preparation of mineral dust samples, or the
430 difference between diverse experimental structures such as the DRIFTS and Knudsen
431 cell in kinetics discussion. In this study, mineral dust particles were in a highly
432 accumulative state in the sample support of Knudsen cell. The many layers of
433 particles in the latter study will hinder the diffusion of gas into the underlayer
434 particles, resulting in the underestimate of γ_{BET} . However, the values herein were
435 comparable to those obtained by the similar DRIFTS setup (Fu et al., 2007),
436 indicating the reliability of our measurements.

437 In addition, the formation rate of sulfate appeared a linear increasing trend as a
438 function of pH cycles. Specifically, the increasing amount of sulfate ions for the
439 IMt-2, NAu-2, SWy-2 and ATD samples after each pH cycle during CP were 7.0×10^{10} ,
440 1.0×10^{11} , 5.0×10^{10} , 3.0×10^{10} , in the order of NAu-2 > IMt-2 > SWy-2 > ATD (Figure
441 4). The multiples factors for $\gamma_{\text{BET}} (\gamma_{\text{geo}})$ were coincided with the total Fe content of
442 these samples: NAu-2 (26.30%) > IMt-2 (5.45%) > SWy-2 (2.36%) > ATD (1.48%).
443 We thus supposed that the SO_2 uptake on these dust samples was closely related to the
444 Fe hosted in the particles.

445 **Figure 4**

446 **3.4 Fe speciation analysis before and after CP.**

447 The fractions of “free-Fe” (including Fe_A and Fe_D) and “structural-Fe” in the
448 mineral particles before and after CP were determined by the CBD extraction (Figure
449 5). In terms of total Fe, the amorphous Fe (Fe_A) (e.g., nanoparticulate and poorly
450 crystalline ferrihydrite) contents of the IMt-2, NAu-2, SWy-2 and ATD samples
451 before CP were 0.7%, 0.5%, 0.7% and 3.8%, respectively. The crystalline Fe

删除的内容: 3

删除的内容: The $\gamma_{\text{BET}} (\gamma_{\text{geo}})$ for IMt-2, NAu-2, SWy-2 and ATD after CP were 2.2 (4.7), 4.1 (19.4), 1.5 (2.7) and 1.4 (2.0) times greater than the corresponding values for those without CP procedure, respectively.

删除的内容: were

删除的内容: 3

删除的内容: 3.4 Morphological change of the mineral particles after CP.

Figure 4 shows the TEM images of the mineral particles before and after CP. As shown in Figure 4 a, c, e and g, the IMt-2, NAu-2, SWy-2 and ATD samples before CP primarily consisted of laminar aluminosilicate with irregular shape and rough morphologies mainly at the micrometer scale, all of which were characterized by various fractions of Fe (1.5%-26.2%), along with minor Mg (0.1%-16.5%), K (0.0%-7.8%) and Ca (0.0%-1.1%). The Fe within the aluminosilicates of the particles was evenly distributed. Besides, some Fe-rich crystal with several hundreds of nanometers in size were found to attach onto the ATD particles, which were identified as $\alpha\text{-Fe}_2\text{O}_3$ (PDF: 33-664) from the typical *d*-spacing analysis of HRTEM (Janney et al., 2000).

After the simulated CP, all of the processed mineral particles showed much smaller size than the ones before CP. For example, the typical IMt-2 and NAu-2 particles after CP (Figure 4 b and d) were $< 1 \mu\text{m}$ in size. Under the TEM, the average Fe content of the individual IMt-2 and SWy-2 particles (Figure 4 b and f) decreased from 5.5% ($\pm 1.9\%$; $n = 50$) to 4.1% ($\pm 1.6\%$; $n = 50$) and from 2.4% ($\pm 0.6\%$; $n = 50$) to 2.1% ($\pm 0.5\%$; $n = 50$), respectively. In addition, the IMt-2 particles after CP showed a heterogeneous distribution of the Fe on the basis of the EDX data. Most of the aluminosilicate in IMt-2 after CP hosted lower Fe content (4.1%), whereas a few of the Fe-rich particles with less Si/Al were observed with irregular shapes at the nanoscale. The TEM images of the NAu-2 and ATD particles after CP (Figure 4 h) showed some pseudo-hexagonal nanoparticles with around 5 nm in diameter. Based on the EDX and SAED analysis, these nanoparticles were Fe-rich and the *d*-spacings was at about 1.5-2.5 Å, all of which were identified to be 2-line ferrihydrite (Janney et al., 2000; Shi et al., 2009).

The TEM observation suggested that CP induced the disintegration of mineral particles and thus produced enhanced surface area, resulting in more active sites available on the particle surfaces for SO_2 uptake. Results of TEM also showed that CP influenced the Fe mineralogy, and lead to the Fe-rich nanoparticle formation, which could partly explain the higher SO_2 uptake on the mineral particles after CP.

Figure 4.

已上移 [1]: Figure 4 shows the TEM images of the mineral after CP. As shown in Figure 4 a, c, e and g, the IMt-2, NAu-2, SWy-2 and ATD samples before CP primarily consisted of laminar aluminosilicate with irregular shape and rough morphologies mainly at the micrometer scale, all of which were characterized by various fractions of Fe (1.5%-26.2%), along with minor Mg (0.1%-16.5%), K (0.0%-7.8%) and Ca (0.0%-1.1%). The Fe within the aluminosilicates of the particles was evenly distributed. Besides, some Fe-rich crystal with several hundreds of nanometers in size were found to attach onto the ATD particles, which were identified as $\alpha\text{-Fe}_2\text{O}_3$ (PDF: 33-664) from the typical *d*-spacing analysis of HRTEM (Janney et al., 2000).

After the simulated CP, all of the processed mineral particles showed much smaller size than the ones before CP. For example, the typical IMt-2 and NAu-2 particles after CP (Figure 4 b and d) were $< 1 \mu\text{m}$ in size. Under the TEM, the average Fe content of the individual IMt-2 and SWy-2 particles (Figure 4 b and f) decreased from 5.5% ($\pm 1.9\%$; $n = 50$) to 4.1% ($\pm 1.6\%$; $n = 50$) and from 2.4% ($\pm 0.6\%$; $n = 50$) to 2.1% ($\pm 0.5\%$; $n = 50$), respectively. In addition, the IMt-2 particles after CP showed a heterogeneous distribution of the Fe on the basis of the EDX data. Most of the aluminosilicate in IMt-2 after CP hosted lower Fe content (4.1%), whereas a few of the Fe-rich particles with less Si/Al were observed with irregular shapes at the nanoscale. The TEM images of the NAu-2 and ATD particles after CP (Figure 4 h) showed some pseudo-hexagonal nanoparticles with

删除的内容: 5

559 (oxyhydr)oxides (Fe_D) (e.g., $\alpha\text{-FeOOH}$ and $\alpha\text{-Fe}_2\text{O}_3$) contents of the IMt-2, NAu-2,
560 SWy-2 and ATD samples before CP were 7.2%, 2.3%, 4.5% and 35.5%, respectively.
561 As a result, the fractions of “structural-Fe” before CP were 92.1%, 97.2%, 94.8% and
562 60.7%, respectively, for IMt-2, NAu-2, SWy-2 and ATD.

563 After CP, the Fe_A contents of the IMt-2, NAu-2, SWy-2 and ATD samples reached
564 1.8%, 1.2%, 1.7% and 24.2%, respectively, which increased by 2.6, 2.4, 2.4 and 6.4
565 times as compared to the ones before CP. The crystalline Fe (oxyhydr)oxides (Fe_D)
566 contents of the samples after CP were not significantly changed as compared to the
567 ones before CP; whereas the content of “structural-Fe” in the Al-Si crystals of the
568 IMt-2, NAu-2, SWy-2 and ATD samples after CP decreased by various degrees, to
569 91.1%, 96.1%, 93.2% and 42.5%, respectively. Previous research had indicated that
570 Fe_A increased as a result of the simulated CP (Shi et al., 2009). Herein, we further
571 proposed that the increased fractions of Fe_A could be mostly transformed from the
572 “structural-Fe” in the aluminosilicate phase of the particles during CP, which is in
573 good agreement with the TEM observation. For example, the Fe_A in the ATD samples
574 increased from 3.8% to 24.2% after CP, accompanied by a sharp decrease of the
575 structural-Fe content from 60.7% to 42.5%.

576 **Figure 5**

577 The Mössbauer spectra and their fitted results are shown in Figure 6. The
578 corresponding hyperfine parameters estimated from the best fitted spectra are
579 presented in Table S3. The central doublet with isomer shift (IS) of 0.37 mm s^{-1} and
580 quadrupole shift (QS) of 0.72 mm s^{-1} were typical for high-spin Fe(III) in octahedral
581 symmetry (Eyre and Dickson, 1995), while the other one with IS of 1.12 mm s^{-1} and
582 QS of 2.65 mm s^{-1} was characteristic of high spin Fe(II) (Hofstetter et al., 2003;
583 Kopcewicz et al., 2015). The two doublet components of the IMt-2, NAu-2, SWy-2

删除的内容: We thus proposed that the increased fractions of Fe_A could be mostly transformed from the “structural-Fe” in the aluminosilicate phase of the particles during CP, which is in good agreement with the TEM observation.

588 and ATD samples before CP were all attributed to different fractions of Fe(III) and
589 Fe(II) in the aluminosilicate crystals, respectively. Before CP, the Fe(II) fraction in the
590 IMt-2, NAu-2, SWy-2 and ATD samples were 34.0 %, 12.9 %, 18.3 % and 29.0 %,
591 respectively (Figure 6 a, c, e and g). Furthermore, the spectra of the ATD sample
592 before CP showed not only two central quadrupole doublets, but also one MHS sextet
593 with IS of 0.39 mm s^{-1} , QS of -0.13 mm s^{-1} and H_f of 51.1 T. The MHS sextet, which
594 shared 31.8 % of the whole area, could be ascribed to $\alpha\text{-Fe}_2\text{O}_3$ (Kopcewicz and
595 Kopcewicz et al., 1991), in agreement with the TEM analysis and “free-Fe”
596 measurement as mentioned previously.

597 After CP, the Fe(II) content of the samples decreased to 31.5 %, 11.6 %, 17.1% and
598 10.9%, respectively, for IMt-2, NAu-2, SWy-2 and ATD (Figure 6 b, d, f and h). It
599 was supposed that the Fe(II) release is more energetically favorable than one of Fe(III)
600 due to the bond strength. As to the ATD sample after CP (Figure 6 h), not only did the
601 Fe(II) fraction decrease from 29.0% to 10.9%, but also the Fe(III) fraction in the
602 aluminosilicates decreased from 39.0% to 33.0%. Meanwhile, the $\alpha\text{-Fe}_2\text{O}_3$ fraction
603 was not significantly changed (31.8% vs. 32.3%). As discussed previously, the Fe
604 mobilization was dependent on the specific chemical bonds. The Fe_D phase in
605 $\alpha\text{-Fe}_2\text{O}_3$ with the strong Fe–O bond was less liable than that embedded in the
606 aluminosilicate lattice (Strehlau et al., 2017). It was well documented that the Fe
607 replacing alkaline elements as the interlayer ions was easy to be mobilized than the Fe
608 bound by covalent bonds in the aluminosilicate matrix (Luo et al., 2005; Cwiertny et
609 al., 2008; Journet et al., 2008). Therefore, the Fe in the aluminosilicate fraction of the
610 mineral particles exhibited varied iron solubility.

611 Particularly, a new quadrupole doublet with IS of 0.67 mm s^{-1} and QS of 1.21 mm
612 s^{-1} was observed in the spectra of the ATD sample after CP (Figure 6 h), which shared

613 23.8% of the total area, and was possibly indicative of the Fe(III) oxide hybridized in
614 the aluminosilicate matrix (Kopcewicz and Kopcewicz, 1991). The “free-Fe”
615 measurement have indicated that the Fe_A fraction of ATD increased by 20.4% after CP,
616 so that this Fe phase was most likely to be amorphous Fe(III) hybridized with Al/Si.
617 In the terms of the other samples after CP, the magnetic signal of the newly formed
618 Fe(III) phase was not detected. It was probably due to the newly formed Fe fractions
619 were not available at sufficiently high level to be clearly resolved by the Mössbauer
620 spectroscopy, and/or the slight signal drift and the poor signal to noise ratio made an
621 unambiguous identification difficult. Herein, the newly formed amorphous Fe(III)
622 phase was supposed to be a reactive Fe-bearing component, of which may contribute
623 significantly to the SO_2 uptake even at a low level.

624 **Figure 6**

625 **3.5 The dissolution-precipitation cycle of the mineral Fe during CP**

626 During the simulated CP experiments, the concentrations of total dissolved Fe (Fe_s),
627 dissolved Fe(II) and Fe(III) released from the particles as a function of time are shown
628 in Figure 7. Similar dissolution trends were observed for all of the samples. One can
629 see that the suspensions at pH 2 induced a rapid increase of Fe_s . Once increasing the
630 pH from 2 to 5 resulted in a rapid and almost complete removal of Fe_s . In fact, only a
631 rather small fraction of the Fe in dusts could be dissolved at pH above 4 (Zuo and
632 Hoigne, 1992). The dissolved Fe precipitated rapidly as insoluble deposit at pH 5.
633 When the suspension pH was again reduced to 2, a steep increase in the Fe_s
634 concentration was measured once again. The fast Fe release was due to the
635 redissolution of the Fe-rich precipitates, which was proposed to be reactive Fe phases
636 (Shi et al., 2009; Shi et al., 2015). Such highly soluble Fe-bearing precipitates have
637 been observed under the TEM, as well as the “free Fe” measurement and Mössbauer

删除的内容: 6

删除的内容: The fast Fe release was due to the redissolution of the Fe-rich precipitates, which was proposed to be reactive Fe phases.

641 characterization.

642 **Figure 7**

643 For each pH cycle during the simulated CP experiment, the overall changes of total
644 released Fe concentrations were reproducible. The Fe ion on the particle surfaces
645 would experience a continuous dissolution-precipitation-redissolution-precipitation
646 process when the pH cycles between pH 2 and pH 5 (cloud-aerosol modes). During
647 this process, the Fe(II) fraction would be transformed to Fe(III). The results shown
648 herein suggested that CP could significantly modify Fe partitioning between dissolved
649 and particulate phases in the real atmosphere. Not only did the increase of specific
650 surface area contribute to the enhanced sulfate formation, but also the highly reactive
651 Fe on the particle surfaces yielded during CP were also responsible for the higher SO₂
652 uptake on the particles after CP.

653 When investigating the NAu-2 sample, once the pH of the clear solution increased
654 from 2 to 5-6, the Fe-bearing nanoparticles separated out from the solution rapidly
655 and precipitate out slowly. It developed an initial yellow color and then an orange
656 colored suspension. The TEM images of the precipitated particles are shown in Figure
657 8. The particles could be categorized into two different types. One type of particle
658 could be characterized as hundreds of nanometers in size, with low Fe but high Si/Al
659 content. The other type displayed particle sizes nearly 1 micrometer, and were Fe-rich
660 but contained a smaller amount of Si/Al components. These bigger particles were
661 ambiguously identified as Na_{0.42}Fe₃Al₆B₃₀₉Si₆O₁₈(OH)_{3.65} (PDF: 89-6506) on the
662 basis of the EDX data and SAED analysis. It is likely that the Al/Si elements also
663 precipitated out along with the Fe.

664 **Figure 8**

665 The Mössbauer spectra of the precipitated Fe-rich particles are shown in Figure 9.
666 Two central doublets were distinguished, with one (48.4%) of $IS = 0.45 \text{ mm s}^{-1}$, $QS =$
667 0.75 mm s^{-1} , and the other (51.6%) of $IS = 0.24 \text{ mm s}^{-1}$, $QS = 0.76 \text{ mm s}^{-1}$. Both of
668 the two doublet components could be attributed to the Fe(III) fraction in the
669 aluminosilicates (Kopcewicz et al., 2015). The results were in good agreement with
670 the TEM observation, which showed that most of these Fe particles were mostly
671 present as the Fe(III) hybridized with Al/Si. The particle size distributions in the
672 suspensions were also determined by dynamic light scattering, as shown in Figure 10.
673 When pH was lower than 2.0, the particles seemed to stabilize below 10 nm in size.
674 These Fe colloids were thought to be a source of soluble Fe (Janney et al., 2000).
675 Once pH increased, the size of precipitated particles quickly increased, even to
676 micro-scale, and the suspension was featured with a polydispersed size distribution.

677 Conclusively, the precipitated Fe were mainly Fe(III) with weak crystal structure
678 and/or ferrihydrite nanoparticle hybridized with Al/Si, which were possibly
679 transformed from the Fe hosted in the aluminosilicate matrix of the particles. The
680 particle surfaces after CP were coated by these reactive Fe to provide more surface
681 OH species, resulting in enhanced SO_2 uptake.

删除的内容: The particle surfaces after CP was coated by these reactive Fe, resulting in enhanced SO_2 uptake.

682 **Figure 9**

683 **Figure 10**

684 **4 Conclusion and implication**

685 Transition metal ions, especially Fe(III), could catalyze SO_2 oxidation rapidly in
686 cloud drops (Harris et al., 2013). This study further confirmed that SO_2 uptake on the
687 mineral particles could be greatly enhanced by CP, possibly more than described
688 previously. The higher uptake coefficient of the particles after CP was not only due to
689 increased surface area, but also resulted from the chemical modification of the particle

删除的内容: during

693 surfaces. The “free-Fe” and Mössbauer analysis suggested that CP triggered newly
694 formation of amorphous Fe particles on the surfaces, of which were mostly
695 transformed from the Fe hosted in the aluminosilicate matrix. TEM showed that the
696 amorphous Fe(III) and/or ferrihydrite nanoparticle were hybridized with Al/Si. In
697 general, the acidity fluctuation during CP enables the dissolution-precipitation cycles
698 of mineral Fe to yielded more reactive Fe, resulting in more SO₂ uptake on the
699 particle surfaces. More SO₂ adsorption further increases the surface acidity of dust
700 particles, in turn leading to higher Fe solubility; again, more sulfate formation. It was
701 thus proposed that there is a positive feedback relative to SO₂ uptake and iron
702 mobilized from mineral particles during CP, therefore enhanced sulfate formation
703 greatly.

704 Our results also serve to explain high sulfate loading in fog-haze episodes of China.
705 It has been recommended that sulfate contributed significantly to the explosive
706 growth of fine particles, thus exacerbating severe fog-haze development (Kasibhatla
707 et al., 1997; Nie et al., 2014; Barrie et al., 2016). Haze and fog within an episode was
708 often found to transform each other at a short time due to the diurnal variation of RH,
709 whereby the haze-fog transition was probably analogous to the aerosol-cloud
710 interaction. Water content of aerosol or fog drops was regulated by RH, and thus
711 allowed the particle acidity fluctuation. Although the aerosol acidity could not be
712 accurately determined from field measurements or calculated using the
713 thermodynamic model, we recognized that the large pH fluctuations between the
714 haze-fog modes could significantly modify the microphysical properties of mineral
715 particles, and triggered formation of reactive Fe particles and thus accelerated sulfate
716 formation via a self-amplifying process, contributing to explosive growth of fine
717 particles at the initial stage of fog-haze events. The data presented herein also

718 highlight that CP provide more bioavailable iron from mineral particle than one
719 expected previously, of which is a key speciation to promote oceanic primary
720 productivity. Results of this study could partly explain the missing source of sulfate
721 and improve agreement between models and field observations.

722 Additionally, previous studies indicated that Fe in pyrogenic aerosols was always
723 presented as liable Fe, such as ferric sulfate and aggregated nanocrystals of magnetite
724 (Fe_3O_4) (Fu et al., 2012), and displayed higher Fe solubility compared to dust
725 (Desboeufs et al., 2005; Sedwick et al., 2007; Ito et al., 2019). Alexander et al.
726 demonstrated that the sulfate formed through metal catalysis was highest over the
727 polluted industrial regions of northern Eurasia, suggesting that the increasing
728 importance of the metal-catalyzed S(IV) oxidation pathway due to anthropogenic
729 emissions (Alexander et al, 2009). With the rapid development of industry and
730 agriculture, the pyrogenic Fe-containing aerosols are indispensable contributors to the
731 atmospheric Fe load in China. Thus, the acidic solution at pH 2 and high sulfate
732 loading of fine particles in severe fog-haze events of China might be more relevant to
733 Fe-containing combustion aerosols than mineral dust. Based on the current findings,
734 not only the potential influences of cloud liquid water content, light, and organic
735 ligands, but also the solubility and speciation of Fe in pyrogenic aerosols will be
736 considered during the simulated CP experiments in the future. A more detailed
737 understanding of the iron-sulfur cycle during CP is therefore critical to estimate
738 accurately the contribution of CP to global sulfate loading and its impact on the
739 climate.

Author contributions. Z.W., H.F. and J.C. designed the experiments, Z.W., T.W., H.F. and L.Z. performed the laboratory experiments. H.F., J.C., L.Z. and V.G. contributed reagents/analytic tools. C.G., V.G. and M.T. gave some valuable suggestions in designing the experiments. Z.W., T.W. and H.F. analyzed data. Z.W. and H.F. wrote the manuscript, with inputs from all coauthors.

Competing interests. The authors declare no conflict of interest.

Acknowledgments. This work was supported by [National Natural Science Foundation of China](#) (Nos. 91744205, 21777025, 21577022, 21177026), [National Key R&D Program of China \(2016YFC0202700\)](#), and [Opening Project of Shanghai Key Laboratory of Atmospheric Particle Pollution and Prevention](#).

删除的内容: National Key R&D Program of China (2016YFC0202700),

删除的内容: International Cooperation Project of Shanghai Municipal Government (15520711200) and

References

- Alexander, B., Park, R. J., Jacob, D. J., and Gong, S.: Transition metal-catalyzed oxidation of atmospheric sulfur: Global implications for the sulfur budget, *J. Geophys. Res.*, 114, D02309, 2009.
- Andreae, M. O., and Rosenfeld, D.: Aerosol-cloud-precipitation interactions. Part 1. The nature and sources of cloud-active aerosols, *Earth Sci. Rev.*, 89, 13-41, 2008.
- Baker, A. R., and Croot, P. L.: Atmospheric and marine controls on aerosol iron solubility in seawater, *Mar. Chem.*, 120, 4-13, 2010.
- Barrie, L. A., Yi, Y., Leitch, W. R., Lohmann, U., Kasibhatla, P., Roelofs, G. J., Wilson, J., McGovern, F., Benkovitz, C., Mélières, M. A., Law, K., Prospero, J., Kritz, M., Bergmann, D., Bridgeman, C., Chin, M., Christensen, J., Easter, R., Feichter, J., Land, C., Jeuken, A.,

- Kjellström, E., Koch, D., and Rasch, P.: A comparison of large-scale atmospheric sulphate aerosol models (COSAM): Overview and highlights, *Tellus B*, 53, 615-645, 2016.
- Behra, P., Sigg, L., and Stumm, W.: Dominating influence of NH₃ on the oxidation of aqueous SO₂: the coupling of NH₃ and SO₂ in atmospheric water, *Atmos. Environ.*, 23, 2691-2707, 1989.
- Cheng, Y. F., Zheng, G. J., Wei, C., Mu, Q., Zheng, B., Wang, Z. B., Gao, M., Zhang, Q., He, K. B., Carmichael, G., Poschl, U., and Su, H.: Reactive nitrogen chemistry in aerosol water as a source of sulfate during haze events in China, *Sci. Adv.*, 2, 1-11, 2016.
- Claquin, T., Schulz, M., and Balkanski, Y. J.: Modeling the mineralogy of atmospheric dust sources, *J. Geophys. Res.-Atmos.*, 104, 22243-22256, 1999.
- Cwiertny, D. M., Baltrusaitis, J., Hunter, G. J., Laskin, A., Scherer, M. M., and Grassian, V. H.: Characterization and acid-mobilization study of iron-containing mineral dust source materials, *J. Geophys. Res.-Atmos.*, 113, D05202, 2008.
- Deguillaume, L., Desboeufs, K. V., Leriche, M., Long, Y., and Chaumerliac, N.: Effect of iron dissolution on cloud chemistry: from laboratory measurements to model results, *Atmos. Pollut. Res.*, 1, 220-228, 2010.
- Desboeufs, K. V., Losno, R., and Colin, J. L.: Factors influencing aerosol solubility during cloud processes, *Atmos. Environ.*, 35, 3529-3537, 2001.
- Desboeufs, K. V., Sofikitis, A., Losno, R., Colin, J. L., and Ausset, P.: Dissolution and solubility of trace metals from natural and anthropogenic aerosol particulate matter, *Chemosphere*, 58, 195-203, 2005.

- Eyre, J. K., and Dickson, D. P. E.: Mössbauer spectroscopy analysis of iron-containing minerals in the Chinese loess, *J. Geophys. Res.*, 100, 17925-17930, 1995.
- Faust, B. C., Hoffmann, M. R., and Bahnemann, D. W.: Photocatalytic oxidation of sulfur dioxide in aqueous suspensions of α -Fe₂O₃, *J. Phys. Chem.*, 93, 6371-6381, 1989.
- Fu, H. B., Wang, X., Wu, H. B., Yin, Y., and Chen, J. M.: Heterogeneous uptake and oxidation of SO₂ on iron oxides, *J. Phys. Chem. C*, 111, 6077-6085, 2007.
- Fu, H. B., Lin, J., Shang, G. F., Dong, W. B., Grassian, V. H., Carmichael, G. R., Li, Y., and Chen, J. M.: Solubility of iron from combustion source particles in acidic media linked to iron speciation, *Environ. Sci. Technol.*, 46, 11119-11127, 2012.
- Formenti, P., Rajot, J. L., Desboeufs, K., Caquineau, S., Chevaillier, S., Nava, S., Gaudichet, A., Journet, E., Triquet, S., Alfaro, S., Chiari, M., Haywood, J., Coe, H., and Highwood, E.: Regional variability of the composition of mineral dust from western Africa: Results from the AMMA SOP0/DABEX and DODO field campaigns, *J. Geophys. Res.*, 113, D00C13, 2008.
- George, C., Ammann, M., D'Anna, B., Donaldson D. J., and Nizkorodov, S. A.: Heterogeneous Photochemistry in the Atmosphere, *Chem. Rev.*, 115, 4218-4258, 2015.
- Goodman, A. L., Li, P., Usher, C. R., and Grassian, V. H.: Heterogeneous uptake of sulfur dioxide on aluminum and magnesium oxide particles, *J. Phys. Chem. A*, 105, 6109-6120, 2001.
- Harris, E., Sinha, B., Foley, S., Crowley, J. N., Borrmann, S., and Hoppe, P.: Sulfur isotope fractionation during heterogeneous oxidation of SO₂ on mineral dust, *Atmos. Chem. Phys.*,

12, 4867-4884, 2012.

Harris, E., Sinha, B., van Pinxteren, D., Tilgner, A., Fomba, K. W., Schneider, J., Roth, A., Gnauk, T., Fahlbusch, B., Mertes, S., Lee, T., Collett, J., Foley, S., Borrmann, S., Hoppe, P., and Herrmann, H.: Enhanced role of transition metal ion catalysis during in-cloud oxidation of SO₂, *Science*, 340, 727-730, 2013.

Herman, L. M. S.: Heterogeneous and homogeneous oxidation of SO₂ in the remote marine atmosphere, *Atmos. Environ.*, 25, 1489-1496, 1991.

Huang, L., Zhao, Y., Li, H., and Chen, Z.: Kinetics of heterogeneous reaction of sulfur dioxide on authentic mineral dust: Effects of relative humidity and hydrogen peroxide, *Environ. Sci. Technol.*, 49, 10797-17805, 2015.

Hofstetter, T. B., Schwarzenbach, R. P., and Haderlein, S. B.: Reactivity of Fe(II) species associated with clay minerals, *Environ. Sci. Technol.*, 37, 519-528, 2003.

Ito, A., Myriokefalitakis, S., Kanakidou, M., Mahowald, N., Scanza, R., Hamilton, D., Baker, A., Jickells, T., Sarin, M., Bikkina, S., Gao, Y., Shelley, R., Buck, C., Landing, W., Bowie, A., Perron, M., Guieu, C., Meskhidze, N., Johnson, M., Feng, Y., Kok, J., Nenes, A. and Duce, R.: Pyrogenic iron: The missing link to high iron solubility in aerosols, *Sci. Adv.*, 5(5), eaau7671, 2019.

Janney, D. E., Cowley, J. M., and Buseck, P. R.: Transmission electron microscopy of synthetic 2- and 6-line ferrihydrite, *Clay Clay Miner.*, 48, 111-119, 2000.

Jickells, T. D., An, Z. S., Andersen, K. K., Baker, A. R., Bergametti, G., Brooks, N., Cao, J. J., Boyd, P. W., Duce, R. A., Hunter, K. A., Kawahata, H., Kubilay, N., laRoche, J., Liss, P. S.,

- Mahowald, N., Prospero, J. M., Ridgwell, A. J., Tegen, I., and Torres, R.: Global iron connections between desert dust, ocean biogeochemistry, and climate, *Science*, 308, 67-71, 2005.
- Journet, E., Desboeufs, K. V., Caquineau, S., and Colin, J.-L.: Mineralogy as a critical factor of dust iron solubility, *Geophys. Res. Lett.*, 35, L07805, 2008.
- Kadar, E., Fisher, A., Stolpe, B., Calabrese, S., Lead, J., Valsami-Jones, E., and Shi, Z.: Colloidal stability of nanoparticles derived from simulated cloud-processed mineral dusts, *Sci. Total. Environ.*, 466-467, 864-870, 2014.
- Kasibhatla, P., Chameides, W. L., and John, J. S.: A three-dimensional global model investigation of seasonal variations in the atmospheric burden of anthropogenic sulfate aerosols, *J. Geophys. Res.-Atmos.*, 102, 3737-3759, 1997.
- Kerminen, V. M., Pirjola, L., Boy, M., Eskola, A., Teinila, K., Laakso, L., Asmi, A., Hienola, J., Lauri, A., Vainio, V., Lehtinen, K., and Kulmala, M.: Interaction between SO₂ and submicron atmospheric particles, *Atmos. Res.*, 54, 41-57, 2000.
- Kolb, C. E., Cox, R. A., Abbatt, J. P. D., Ammann, M., Davis, E. J., Donaldson, D. J., Garrett, B. C., George, C., Griffiths, P. T., Hanson, D. R., Kulmala, M., McFiggans, G., Pöschl, U., Riipinen, I., Rossi, M. J., Rudich, Y., Wagner, P. E., Winkler, P. M., Worsnop, D. R., and O'Dowd, C. D.: An overview of current issues in the uptake of atmospheric trace gases by aerosols and clouds, *Atmos. Chem. Phys.*, 10, 10561-10605, 2010.
- Kong, L. D., Zhao, X., Sun, Z. Y., Yang, Y. W., Fu, H. B., Zhang, S. C., Cheng, T. T., Yang, X., Wang, L., and Chen, J. M.: The effects of nitrate on the heterogeneous uptake of sulfur

- dioxide on hematite, *Atmos. Chem. Phys.*, 14, 9451-9467, 2014.
- Kopcewicz, B., and Kopcewicz, M.: Mössbauer study of iron-containing atmospheric aerosols, *Struct. Chem.*, 2, 303-312, 1991.
- Kopcewicz, B., Kopcewicz, M., and Pietruczuk, A.: The Mössbauer study of atmospheric iron-containing aerosol in the coarse and PM_{2.5} fractions measured in rural site, *Chemosphere*, 131, 9-16, 2015.
- Lafon, S., Rajot, J.-L., Alfaro, S. C., and Gaudichet, A.: Quantification of iron oxides in desert aerosol, *Atmos. Environ.*, 38, 1211-1218, 2004.
- Lelieveld, J., and Heintzenberg, J.: Sulfate cooling effect on climate through in-cloud oxidation of anthropogenic SO₂, *Science*, 258, 117-120, 1992.
- Luo, C., Mahowald, N. M., Meskhidze, N., Chen, Y., Siefert, R. L., Baker, A. R., and Johansen, A. M.: Estimation of iron solubility from observations and a global aerosol model, *J. Geophys. Res.*, 110, D23, 2005.
- Luo, C., Mahowald, N., Bond, T., Chuang, P. Y., Artaxo, P., Siefert, R., Chen, Y., and Schauer, J.: Combustion iron distribution and deposition, *Global Biogeochem. Cycles*, 22, GB1012, 2008.
- Luria, M., and Sievering, H.: Heterogeneous and homogeneous oxidation of SO₂ in the remote marine atmosphere, *Atmos. Environ.*, 25, 1489-1496, 1991.
- Ma, Q., He, H., and Liu, Y.: In situ DRIFTS study of hygroscopic behavior of mineral aerosol, *J. Environ. Sci.*, 22, 555-560, 2010.
- Mackie, D. S.: Simulating the cloud processing of iron in Australian dust: pH and dust

concentration, *Geophys. Res. Lett.*, 32, L06809, 2005.

Mahowald, N. M., Baker, A. R., Bergametti, G., Brooks, N., Duce, R. A., Jickells, T. D., Kubilay, N., Prospero, J. M., and Tegen, I.: Atmospheric global dust cycle and iron inputs to the ocean. *Global Biogeochem. Cycles*, 19, GB4025, 2005.

Maters, E. C., Delmelle, P., and Bonneville, S.: Atmospheric processing of volcanic glass: Effects on iron solubility and redox speciation. *Environ. Sci. Technol.*, 50 (10), 5033-5040, 2016.

Meskhidze, N.: Iron mobilization in mineral dust: Can anthropogenic SO₂ emissions affect ocean productivity? *Geophys. Res. Lett.*, 30, 1-2, 2003.

Nanayakkara, C. E., Pettibone, J., and Grassian, V. H.: Sulfur dioxide adsorption and photooxidation on isotopically-labeled titanium dioxide nanoparticle surfaces: Roles of surface hydroxyl groups and adsorbed water in the formation and stability of adsorbed sulfite and sulfate, *Phys. Chem. Chem. Phys.*, 14, 6957-6966, 2012.

Nie, W., Ding, A. J., Wang, T., Kerminen, V., George, C., Xue, L. K., Wang, W. X., Zhang, Q. Z., Petäjä, T., Qi, X. M., Gao, X. M., Wang, X. F., Yang, X. Q., Fu, C. B., and Kulmala, M.: Polluted dust promotes new particle formation and growth, *Sci. rep.*, 4, 6634, 2014.

Peak, D., Ford, R. G., and Sparks, D. L.: An in situ ATR-FTIR investigation of sulfate bonding mechanisms on goethite, *J. Colloid Interface Sci.*, 218, 289-299, 1999.

Pruppacher, H. R., Jaenicke, R.: The processing of water-vapor and aerosols by atmospheric clouds, a global estimate, *Atmos. Res.*, 38, 283-295, 1995.

Rubasinghege, G., Lentz, R. W., Scherer, M. M., and Grassian, V. H.: Simulated atmospheric

删除的内容:

- processing of iron oxyhydroxide minerals at low pH: roles of particle size and acid anion in iron dissolution, *Proc. Natl. Acad. Sci. U. S. A.*, 107, 6628-6633, 2010.
- Sedwick, P. N., Sholkovitz, E. R., and Church, T. M.: Impact of anthropogenic combustion emissions on the fractional solubility of aerosol iron: Evidence from the Sargasso Sea, *Geochem. Geophys. Geosyst.*, 8, Q10Q06, 2007.
- Shi, Z., Bonneville, S., Krom, M. D., Carslaw, K. S., Jickells, T. D., Baker, A. R., and Benning, L. G.: Iron dissolution kinetics of mineral dust at low pH during simulated atmospheric processing, *Atmos. Chem. Phys.*, 11, 995-1007, 2011.
- Shi, Z., Krom, M. D., Bonneville, S., Baker, A. R., Jickells, T. D., and Benning, L. G.: Formation of iron nanoparticles and increase in iron reactivity in mineral dust during simulated cloud processing, *Environ. Sci. Technol.*, 43, 6592-6596, 2009.
- Shi, Z., Krom, M. D., Bonneville, S., Baker, A. R., Bristow, C., Drake, N., Mann, G., Carslaw, K., McQuaid, J. B., Jickells, T., and Benning, L. G.: Influence of chemical weathering and aging of iron oxides on the potential iron solubility of Saharan dust during simulated atmospheric processing, *Global Biogeochem. Cycles*, 25, GB2010, 2011.
- Shi, Z., Krom, M. D., Bonneville, S., and Benning, L. G.: Atmospheric processing outside clouds increases soluble iron in mineral dust, *Environ. Sci. Technol.*, 49, 1472-1477, 2015.
- Siefert, R. L., Johansen, A. M., Hoffmann, M. R., and Pehkonen, S. O.: Measurements of trace metal (Fe, Cu, Mn, Cr) oxidation states in fog and stratus clouds, *J. Air Waste Manage.*, 48(2), 128-143, 1998.
- Spokes, L. J., Jickells, T. D., and Lim, B.: Solubilization of aerosol trace-metals by cloud

- processing - a laboratory study, *Geochim. Cosmochim. Acta.*, 58, 3281-3287, 1994.
- Strehlau, J. H., Schultz, J. D., Vindedahl, A. M., Arnold, W. A., and Penn, R. L.: Effect of nonreactive kaolinite on 4-chloronitrobenzene reduction by Fe(II) in goethite-kaolinite heterogeneous suspensions, *Environ. Sci.: Nano*, 4, 325-334, 2017.
- Sun, Y. L., Jiang, Q., Wang, Z. F., Fu, P. Q., Li, J., Yang, T., and Yin, Y.: Investigation of the sources and evolution processes of severe haze pollution in Beijing in January 2013, *J. Geophys. Res.-Atmos.*, 119, 4380-4398, 2014.
- Ullerstam, M., Johnson, M. S., Vogt, R., and Ljungstrom, E.: DRIFTS and Knudsen cell study of the heterogeneous reactivity of SO₂ and NO₂ on mineral dust, *Atmos. Chem. Phys.*, 3, 2043-2051, 2003.
- Usher, C. R., Al-Hosney, H., Carlos-Cuellar, S., and Grassian, V. H.: A laboratory study of the heterogeneous uptake and oxidation of sulfur dioxide on mineral dust particles, *J. Geophys. Res.-Atmos.*, 107, 161-169, 2002.
- Usher, C. R., Michel, A. E., and Grassian, V. H.: Reactions on mineral dust, *Chem. rev.*, 103, 4883-4940, 2003.
- Viollier, E., Inglett, P. W., Hunter, K., Roychoudhury, A. N., and Van Cappellen, P.: The ferrozine method revisited: Fe(II)/Fe(III) determination in natural waters, *Appl. Geochem.*, 15, 785-790, 2000.
- Wang, G., Wang, H., Yu, Y., Gao, S., Feng, J., Gao, S., and Wang, L.: Chemical characterization of water-soluble components of PM₁₀ and PM_{2.5} atmospheric aerosols in five locations of Nanjing, China, *Atmos. Environ.*, 37, 2893-2902, 2003.

- Wang, Y., Zhang, Q., Jiang, J., Zhou, W., Wang, B., He, K., Duan, F., Zhang, Q., Philip, S., and Xie, Y.: Enhanced sulfate formation during China's severe winter haze episode in January 2013 missing from current models, *J. Geophys. Res.-Atmos.*, 119, 10425-10440, 2014.
- Wu, L. Y., Tong, S. R., Wang, W. G., and Ge, M. F.: Effects of temperature on the heterogeneous oxidation of sulfur dioxide by ozone on calcium carbonate, *Atmos. Chem. Phys.*, 11, 6593-6605, 2011.
- Wurzler, S., Reisin, T. G., and Levin, Z.: Modification of mineral dust particles by cloud processing and subsequent effects on drop size distributions, *J. Geophys. Res.-Atmos.*, 105, 4501-4512, 2000.
- Yang, W., He, H., Ma, Q., Ma, J., Liu, Y., Liu, P., and Mu, Y.: Synergistic formation of sulfate and ammonium resulting from reaction between SO₂ and NH₃ on typical mineral dust, *Phys. Chem. Chem. Phys.*, 18, 956-964, 2016.
- Yang, W., Zhang, J., Ma, Q., Zhao, Y., Liu, Y., and He, H.: Heterogeneous reaction of SO₂ on manganese oxides: the effect of crystal structure and relative humidity, *Sci. rep.*, 7, 4550, 2017.
- Zhang, X., Zhuang, G., Chen, J., Wang, Y., Wang, X., An, Z., and Zhang, P.: Heterogeneous reactions of sulfur dioxide on typical mineral particles, *J. Phys. Chem. B*, 110, 12588-12596, 2006.
- Zhao, X., Kong, L., Sun, Z., Ding, X., Cheng, T., Yang, X., and Chen, J.: Interactions between heterogeneous uptake and adsorption of sulfur dioxide and acetaldehyde on hematite, *J.*

Phys. Chem. A, 119, 4001-4008, 2015.

Zhao, Y., Liu, Y., Ma, J., Ma, Q., and He, H.: Heterogeneous reaction of SO₂ with soot: The roles of relative humidity and surface composition of soot in surface sulfate formation, Atmos. Environ., 152, 465-476, 2017.

Zhu, X., Prospero, J. M., Savoie, D. L., Millero, F. J., Zika, R. G., and Saltzman, E. S.: Photoreduction of iron(III) in marine mineral aerosol solutions, J. Geophys. Res.-Atmos., 98, 9039-9046, 1993.

Zhuang, G. S., Yi, Z., Duce, R. A., and Brown, P. R.: Link between iron and sulfur cycles suggested by detection of Fe(II) in remote marine aerosols, Nature, 355 (6360), 537-539, 1992.

Zuo, Y. G., and Hoigne, J.: Formation of hydrogen-peroxide and depletion of oxalic-acid in atmospheric water by photolysis of iron(III) oxalato complexes, Environ. Sci. Technol., 26, 1014-1022, 1992.

Captions of Figures and Tables

Figure 1. Comparison of morphologies and chemical properties for samples collected before and after CP using TEM. The dotted circles indicate the positions of the electron beam for the HRTEM images and SAED patterns. Elements of the detected parts of individual particles are also presented. Square brackets indicate mass percent of iron. The iron species were identified by the Miller indices and the SAED patterns. (a) IMt-2 particles characterized by high fractions of Al and Si, along with other crustal elements including Mg, K and Fe. (b) IMt-2 particles after CP were almost all less than 1 μ m in size. Some Fe-rich particles with less Si and Al were observed on nanoscale dimension. (c) NAu-2 particles with high Fe/Si-ratios, contain Mg, Al and Ca elements. (d) NAu-2 particles after CP were much smaller than the ones before CP. Some ferrihydrite clusters were observed and were attached on the surface of the NAu-2 particles after CP. (e) Typical SWy-2 particles were Al/Si-rich, containing Fe, Mg and Ca elements. (f) TEM images of the SWy-2 particles after CP appeared smaller than the particles before CP. (g) The Si/Al-rich crystal in ATD particles was aluminosilicate with low content of Fe, and a typical of the α -Fe₂O₃ particles (PDF: 33-664) was found to attach onto the aluminosilicate surface. (h) The pseudo-hexagonal nanoparticles were observed to on the surface of α -Fe₂O₃ crystal among the ATD particles. The SAED lattice constant of these nanoparticles were found to be very close to that of 2-line ferrihydrite.

Figure 2. Comparison of the DRIFT spectra of mineral dust samples upon exposure to SO₂ for 45 min before and after CP. Data for IMt-2 (a and b), NAu-2 (c and d), SWy-2 (e and f), ATD (g and h), are shown in the ranges of 4000 to 1250 cm⁻¹ and 1250 to 1000 cm⁻¹, respectively.

已移动(插入) [2]

已下移 [3]: Comparison of the DRIFT spectra of mineral dust samples upon exposure to SO₂ for 45 min before and after CP. Data for IMt-2 (a and b), NAu-2 (c and d), SWy-2 (e and f), ATD (g and h), are shown in the ranges of 4000 to 1250 cm⁻¹ and 1250 to 1000 cm⁻¹, respectively.

已移动(插入) [3]

删除的内容: Comparison of the integrated areas on DRIFTS spectra in the range of 1250-1000 cm⁻¹ for the sulfate species formed on the samples before and after CP.

Figure 3. Comparison of the integrated areas on DRIFTS spectra in the range of 1250-1000 cm^{-1} for the sulfate species formed on the samples before and after CP.

Table 1. Sulfate formation rates and uptake coefficients of SO_2 on particle samples before and after CP.

Figure 4. Comparison of the sulfate formation rates as a function of pH cycle.

Figure 5. The fractions of “free-Fe” (Fe_A and Fe_D) and “structural-Fe” were measured by the chemical CBD extractions for the samples before and after CP. Results are present as relative percentage of Fe_T .

Figure 6. Mössbauer spectroscopy measured for samples. IMt-2 before and after CP (a and b), NAu-2 before and after CP (c and d), SWy-2 before and after CP (e and f), ATD before and after CP (g and h). Experimental data were fit using a least-squares fitting-program. The IS values were relative to α -Fe at RT. Prominent spectral features associated with different iron species are indicated.

Figure 7. The concentrations of Fe_s , dissolved Fe(II) and Fe(III) in the suspensions measured over 144 h in the solution cycled between pH 2 and pH 5 for IMt-2 (a), NAu-2 (b), SWy-2 (c) and ATD (d), respectively.

Figure 8. TEM images of the newly formed particles in the precipitation experiment. Based on the TEM-EDX measurement and SAED analysis, these particles could be categorized into two different types, which were circled in Figure 8 a. The typical sizes of the first type were hundreds of nanometers. The enlarged images are displayed in Figure 8 b, c and d. The insert EDX data and SAED image confirmed that they were poor crystalline aluminosilicate with low Fe but high Si/Al content. The second type (Figure 8 e, f and g) were Fe-rich but with less amount of Si/Al, which were nearly 1 micrometer in size. Based on the EDX data and the SAED

已下移 [4]: Table 1. Sulfate formation rates and uptake coefficients of SO_2 on particle samples before and after CP. .

删除的内容: Comparison of the sulfate formation rates as a function of pH cycle.

已移动(插入) [4]

已上移 [2]: Comparison of morphologies and chemical properties for samples collected before and after CP using TEM. The dotted circles indicate the positions of the electron beam for the HRTEM images and SAED patterns. Elements of the detected parts of individual particles are also presented. Square brackets indicate mass percent of iron. The iron species were identified by the Miller indices and the SAED patterns. (a) IMt-2 particles characterized by high fractions of Al and Si, along with other crustal elements including Mg, K and Fe. (b) IMt-2 particles after CP were almost all less than 1 μm in size. Some Fe-rich particles with less Si and Al were observed on nanoscale dimension. (c) NAu-2 particles with high Fe/Si-ratios, contain Mg, Al and Ca elements. (d) NAu-2 particles after CP were much smaller than the ones before CP. Some ferrihydrite clusters were observed and were attached on the surface of the NAu-2 particles after CP. (e) Typical SWy-2 particles were Al/Si-rich, containing Fe, Mg and Ca elements. (f) TEM images of the SWy-2 particles after CP appeared smaller than the particles before CP. (g) The Si/Al-rich crystal in ATD particles was aluminosilicate with low content of Fe, and a typical of the α - Fe_2O_3 particles (PDF: 33-664) was found to attach onto the aluminosilicate surface. (h) The pseudohexagonal nanoparticles were observed to on the surface of α - Fe_2O_3 crystal among the ATD particles. The SAED lattice constant of these nanoparticles were found to be very close to that of 2-line ferrihydrite.

analysis, these bigger particles were ambiguously identified as $\text{Na}_{0.42}\text{Fe}_3\text{Al}_6\text{B}_{309}\text{Si}_6\text{O}_{18}(\text{OH})_{3.65}$ (PDF: 89-6506).

Figure 9. Mössbauer spectroscopy measured at RT for the neo-formed particles collected in the precipitation experiment.

Figure 10. During the precipitation experiment, the particle size distributions in the suspensions were determined by dynamic light scattering. The presented size distributions are characteristic of neo-formed nanoparticles or microparticles as the suspension pH raised from 1.0 to 3.8.

Figure 1

已移动(插入) [5]

删除的内容: 4

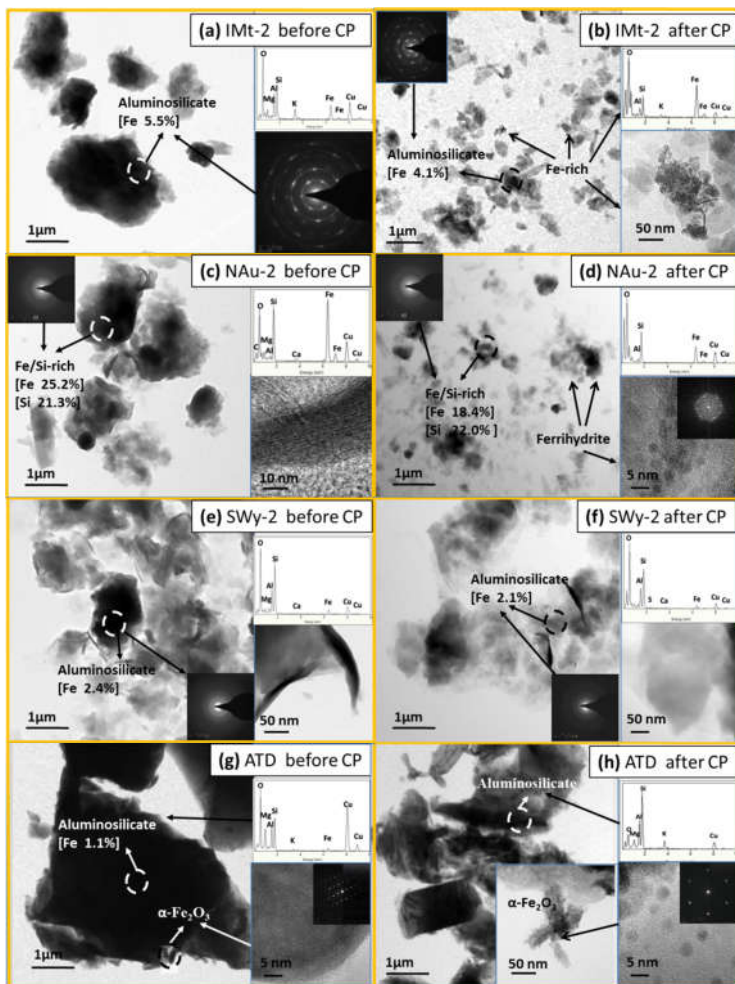


Figure 2

删除的内容: 1

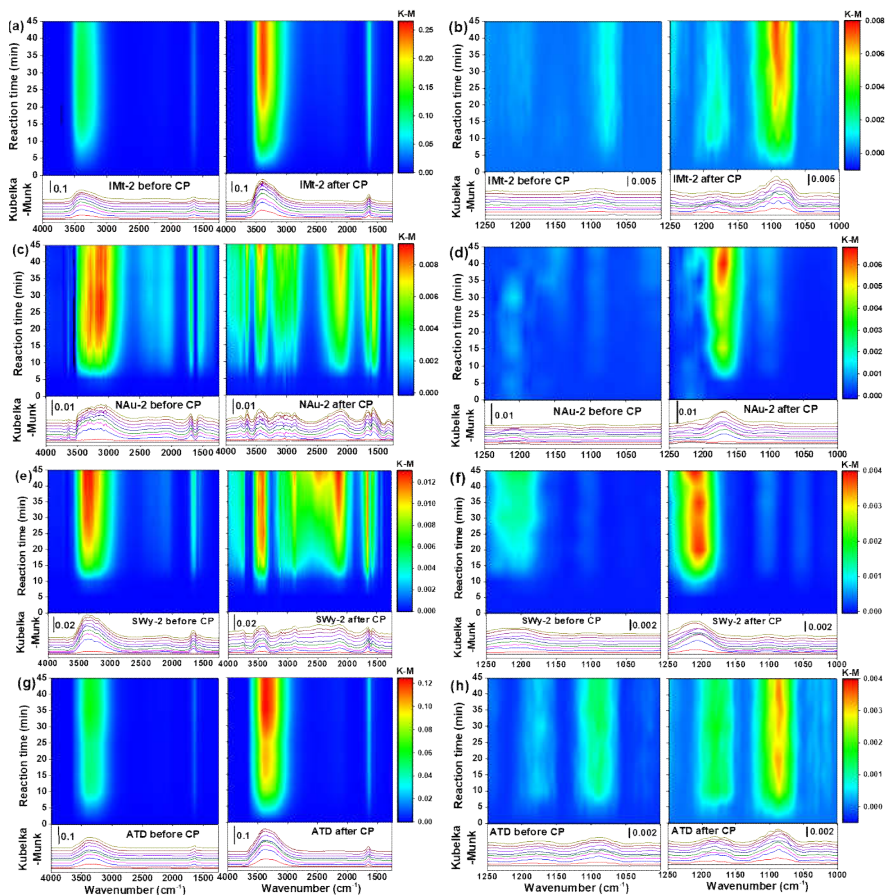


Figure 3

删除的内容: 2

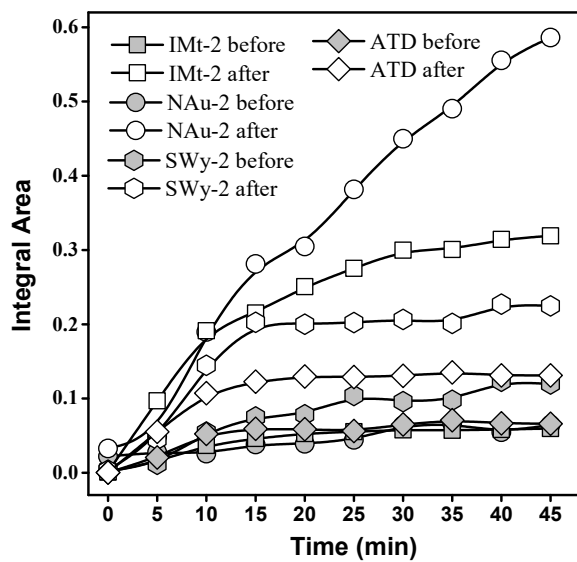


Table 1

Samples	A_{BET} (m^2)	Sulfate formation rate (ions s^{-1}) ($\times 10^{10}$)	$A_{\text{geometric}}$ (m^2) ($\times 10^{-5}$)	γ_{BET} ($\times 10^{-12}$)	$\gamma_{\text{geometric}}$ ($\times 10^{-7}$)
IMt-2 before CP	0.770	6.13	1.95	2.62	1.03
IMt-2 after CP	1.640	28.72	1.95	5.76	4.85
NAu-2 before CP	0.790	1.80	1.95	0.75	0.30
NAu-2 after CP	3.749	34.57	1.95	3.06	5.83
SWy-2 before CP	0.906	10.20	1.95	3.70	1.72
SWy-2 after CP	1.631	27.19	1.95	5.49	4.59
ATD before CP	0.166	8.11	1.95	16.05	1.37
ATD after CP	0.241	16.33	1.95	22.33	2.76

删除的内容: g^{-1}

删除的内容: 20.1 ± 1.5

删除的内容: 32.0 ± 2.6

删除的内容: 19.8 ± 1.3

删除的内容: 93.7 ± 7.5

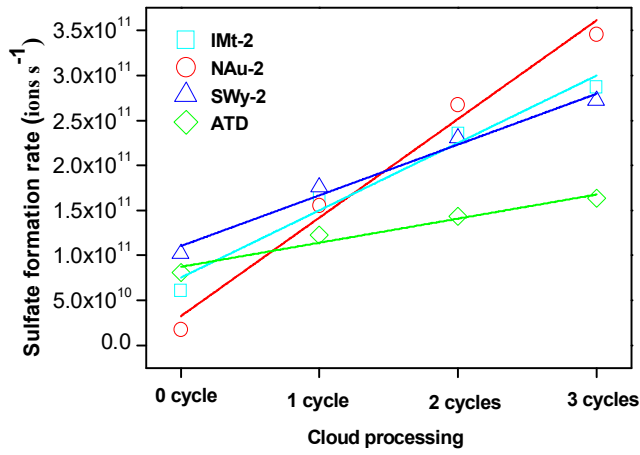
删除的内容: 22.6 ± 2.3

删除的内容: 40.8 ± 1.5

删除的内容: 4.3 ± 0.3

删除的内容: 6.5 ± 1.0

Figure 4



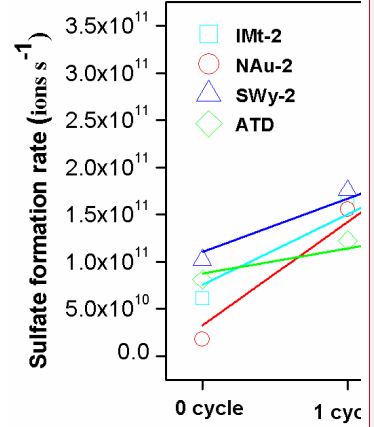
删除的内容: 3

域代码已更改

带格式的: 字体: 加粗

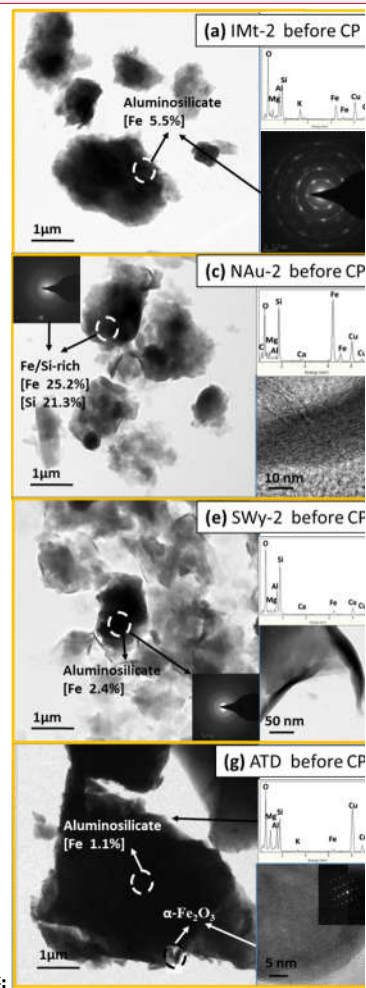
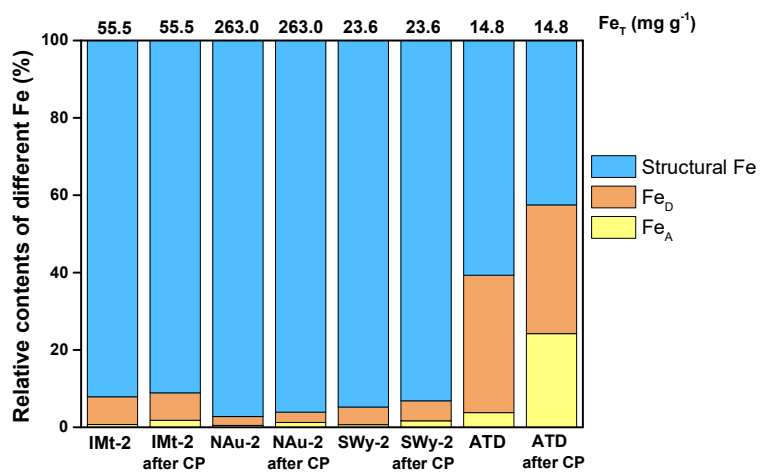
已上移 [5]: Figure 4 .

分页符



删除的内容:

Figure 5



删除的内容:

—分页符—

Figure 6

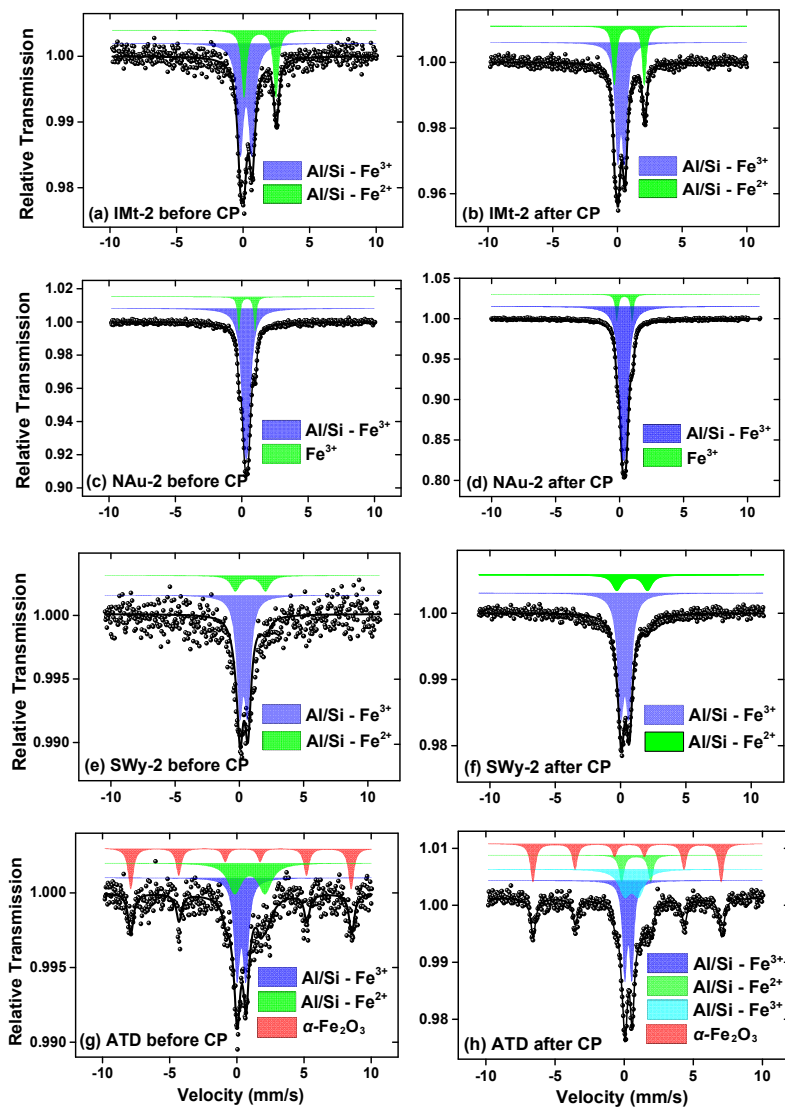


Figure 7

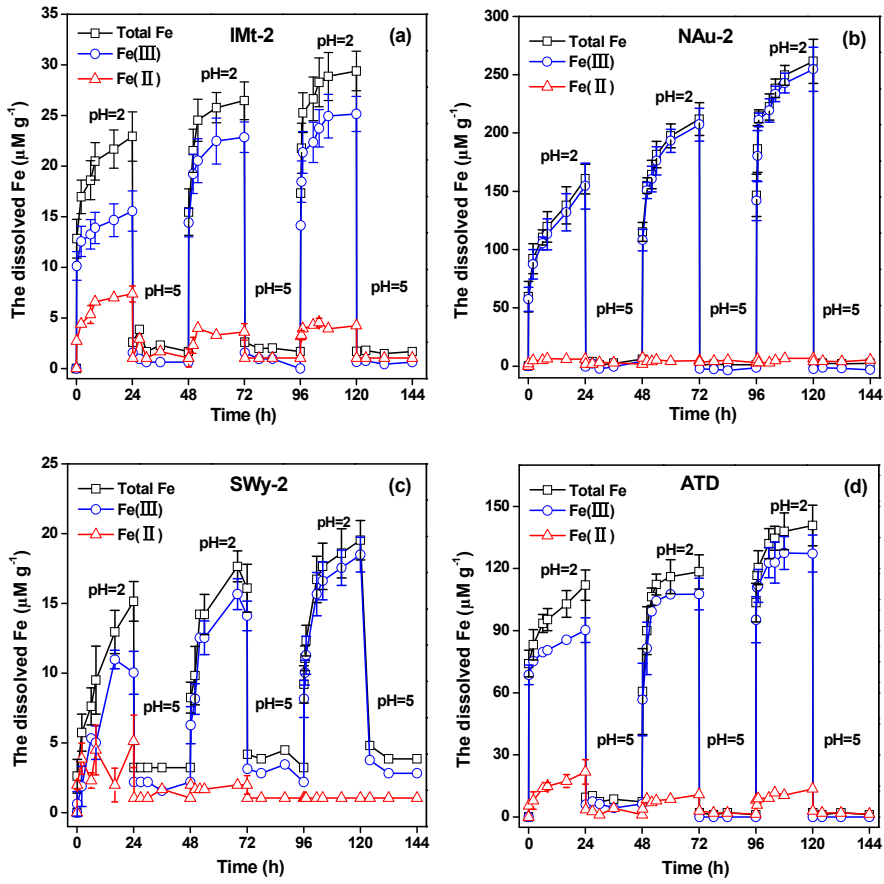


Figure 8

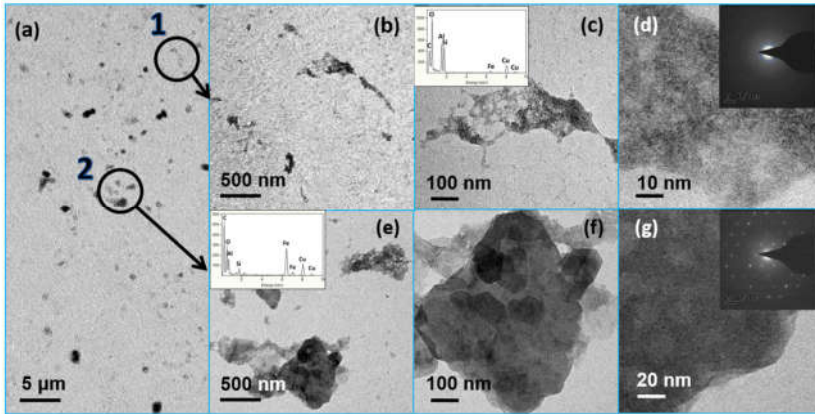


Figure 9

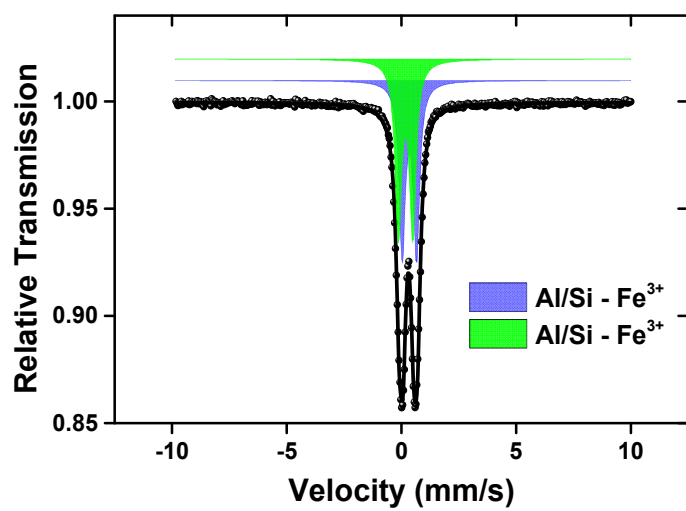


Figure 10

